Atmospheric Environment 214 (2019) 116828

Contents lists available at ScienceDirect

Atmospheric Environment

journal homepage: www.elsevier.com/locate/atmosenv

Performance of a dust model to predict the vertical mass concentration of an extreme Saharan dust event in the Iberian Peninsula: Comparison with continuous, elastic, polarization-sensitive lidars

Carmen Córdoba-Jabonero[a,*], Michaël Sicard[b,c], Ana del Águila[a,1], Marcos Jiménez[d], María-Paz Zorzano[e,f]

[a] *Instituto Nacional de Técnica Aeroespacial (INTA), Área de Investigación e Instrumentación Atmosférica, Ctra. Ajalvir, Km. 4, Torrejón de Ardoz, 28850, Madrid, Spain*
[b] *CommSensLab, Dept. of Signal Theory and Communications, Universitat Politècnica de Catalunya (UPC), Barcelona, Spain*
[c] *Ciències i Tecnologies de l'Espai-Centre de Recerca de l'Aeronàutica i de l'Espai/Institut d'Estudis Espacials de Catalunya (CTE-CRAE/IEEC), Universitat Politècnica de Catalunya (UPC), Barcelona, Spain*
[d] *Instituto Nacional de Técnica Aeroespacial (INTA), Área de Sistemas de Teledetección, Ctra. Ajalvir, Km. 4, Torrejón de Ardoz, Madrid, Spain*
[e] *Centro de Astrobiología (CSIC-INTA), Ctra. Ajalvir, Km. 4, Torrejón de Ardoz, 28850, Madrid, Spain*
[f] *Department of Computer Science, Electrical and Space Engineering, Luleå University of Technology, Luleå, Sweden*

GRAPHICAL ABSTRACT

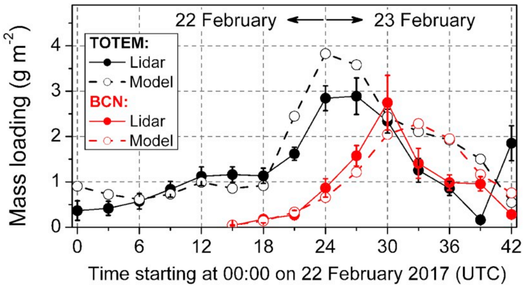

ARTICLE INFO

Keywords:
Dust
LIDAR observations
Mass concentration
Mass extinction efficiency
Model performance

ABSTRACT

An intense dusty event unusually occurred in wintertime over the Iberian Peninsula was detected over two Spanish NASA/MPLNET sites: the temporary Torrejón Observational Tower for Environmental Monitoring (TOTEM, 40.5°N 3.5°W) and the Barcelona station (BCN, 41.4°N 2.1°E). The highest dust incidence was observed from 22 to 23 February 2017; this two-day dusty scenario is examined in order to evaluate the performance of the operational NMMB/BSC-Dust model on forecasted mass concentration profiling in comparison with polarized Micro-Pulse (P-MPL) mass estimates for dust particles. First, the optical properties of the dust (DD) were effectively separated from the non-dust (ND) component by using the combined P-MPL/POLIPHON method. Lidar-derived DD optical depths reached maximums of 1.6–1.7 (± 0.1) at both stations. Typical features for dust were obtained: linear particle depolarization ratios between 0.3 and 0.4, and lidar ratios in the range of 41–70 sr and 36–66 sr, respectively, for TOTEM and BCN. Lower AERONET Ångström exponents were reported for TOTEM (0.12 ± 0.04) than at BCN (0.5 ± 0.3). HYSPLIT back-trajectory analysis showed air masses coming from the Sahara region, mostly transporting dust particles. AERONET-derived Mass Extinction Efficiencies (MEE) under dusty conditions were used for the extinction-to-mass conversion procedure as applied to the P-MPL measurements: MEE values were lower at TOTEM (0.57 ± 0.01 m^2 g^{-1}) than those found at BCN

---

[*] Corresponding author.
E-mail address: cordobajc@inta.es (C. Córdoba-Jabonero).
[1] Present address: Remote Sensing Technology Institute, German Aerospace Centre (DLR), Oberpfaffenhofen, Germany.

https://doi.org/10.1016/j.atmosenv.2019.116828
Received 22 December 2018; Received in revised form 30 June 2019; Accepted 9 July 2019

($0.87 \pm 0.10\,\mathrm{m^2\,g^{-1}}$). Those results reveal that dust particles were predominantly larger at TOTEM than those observed at BCN, and a longer transport of dust particles from the Sahara sources to BCN could favour a higher gravitational settling of coarser particles before reaching BCN than TOTEM. A comparative analysis between profiles as obtained from the lidar DD component of the mass concentration and those forecasted by the NMMB/BSC-Dust model (25 available dusty profiles) was performed. The degree of agreement between both datasets was determined by the percentage of dusty cases satisfying selected model performance criteria (favourable cases) of two proxies: the Mean Fractional Bias, *MFB*, and the correlation coefficient, *CC*. A good agreement is found (72% and 76%, respectively, of favourable cases); however, large discrepancies are found at low altitudes between the dust model and the lidar observations, mostly at early stages of the arrival of the dust intrusion. Higher model-derived centre-of-mass (CoM) heights are found in 60% of the cases (with differences $< 15\%$ w.r.t. the lidar CoM, whose values ranged between 1.8 and 2.3 km height). In addition, modelled mass loading (ML) values were generally higher than the lidar-derived ones. However, the evolution of the mass loading along the two days, 22 and 23 February, was rather similar for both the model forecasting and lidar observations at both stations. The relative ML differences ($< 50\%$) of the mass loading represented 60% of all cases. Discrepancies can be based on the uncertainties in the lidar retrievals (mainly, the use of single extinction-to-mass conversion factors). In general, a moderately good agreement is observed between the P-MPL-derived dust mass concentration profiles and the NMMB/BSC-Dust model ones at both sites; large discrepancies are found at lower altitudes, plausibly due to a lower sedimentation of dust particles coming from upper layers by gravitational settling than that introduced by the NMMB/BSC-Dust model in the simulations. The methodology described for the dust model evaluation against the continuous P-MPL observations can be easily adopted for an operational use of the NMMB/BSC-Dust model for forecasting the mass concentration profiling in frequently dust-affected regions with serious climate and environmental implications, as long as a typical MEE for dust could be accurately specified. Hence, a statistical analysis for determining AERONET-based MEE values over the Iberian Peninsula is on-going.

1. Introduction

As the world has warmed, the Earth temperature increase has triggered many other changes to the Earth's climate. Changes in extreme weather and climate events, such as heat waves, droughts (Sillmann et al., 2013) and heavy downpours (Liu et al., 2015), are the primary way that most people experience climate change. Human-induced climate change has already increased the number and strength of some of these extreme events. Other extreme climate events, less known by the general public because their impact is not as direct as the ones of the phenomena just mentioned, may also be altered by climate change in terms of seasonality, frequency and intensity. In some cases, this alteration can be evidenced through long-term climatological measurements but its relationship with climate change is often far from being straightforward. This hypothetical relationship is still one of the open questions raised by scientists around the world about the future of the climate (WMO, 2011).

An example of these extreme climate events is, e.g., desert dust storms and their long-range transport. At global scale, the largest source of mineral dust is the arid and semi-arid region of the Sahara-Sahel-Chad corridor in the northern hemisphere (Prospero et al., 2002; Moreno et al., 2006). The long-range transport of airborne mineral dust particles from this region is driven by the atmospheric circulation over north-western Africa which is mainly controlled by the northeast trade winds and by the mid-tropospheric Saharan Air Layer. Along the year, the direction of the dust plume transport, its extension and strength vary accordingly to the displacement of the Inter-Tropical Convergence Zone (ITCZ) (Prospero et al., 1981) and the insolation and temperatures over the Sahara-Sahel area (Bergametti et al., 1989). In winter, when the ITCZ is at its southernmost position, dust originated in Sahara and Sahel deserts is transported towards the tropical Atlantic Ocean by northeast trade winds (Alonso-Pérez et al., 2011), while in summer such trade winds are more constrained owing to the northern displacement of the ITCZ (Prospero et al., 1981). For these reasons, the direction of the mineral dust plume transport, its extension and strength are highly seasonal-dependent. At the scale of the European continent and of the Mediterranean Basin in particular, it is now well known that a clear summer prevalence of dust events is observed in the western Mediterranean with low occurrence of extreme episodes. No seasonal trends with moderate-intensity events dominate in the central Basin; and the prevalence of dust events is observed in autumn-spring with occurrence of various extreme episodes throughout the year in the eastern Basin (Querol et al., 1998, 2009; Rodríguez et al., 2001; Escudero et al., 2005; Pey et al., 2013; Cachorro et al., 2016; Gkikas et al., 2016; Sicard et al., 2016).

In the last decade an increasing number of works have reported statistics and tendency of intense (i.e. strong and extreme) Saharan dust events in the Mediterranean Basin. If one considers all aerosol types, Papadimas et al. (2008) have shown with 6 years (2000–2006) of MODIS data over the whole Mediterranean Basin that the regional mean visible aerosol optical depth (AOD) over land and ocean has decreased by 20% in relative percentage terms. They found that this tendency is not uniform over the whole basin and that it appears mainly in the western part. There, the summer AOD has decreased by 14% and the winter AOD has increased by 19%. While the summer decrease is explained by decreased emission rates of anthropogenic pollution, the winter increase is related to decreased precipitation associated with an increasing tendency of the North Atlantic Oscillation (NAO) index, and thus indirectly to dust, whose transport is strongly affected by the NAO (Moulin et al., 1998). If one now considers only mineral dust, Gkikas et al. (2013) have shown with different satellite databases that the frequency of strong and extreme mineral dust events over the whole Mediterranean Basin has decreased over land between 2000 and 2007, independently of the season, whereas their intensity had on average no marked tendency.

As far as frequency is concerned, the finding of Gkikas et al. (2013) is also observed above the Iberian Peninsula (IP) by Cachorro et al. (2016) who found a decrease of mineral dust events from all types with data from the Aerosol Robotic Network (AERONET) (Holben et al., 1998) in the north-central area of the IP over the period 2003–2014. Besides, they also found for the same period that the intensity of mineral dust measured in terms of AOD for all types of events decreased by 50%. The latter study suggests a decrease in mineral dust events over the IP in terms of both frequency and intensity, and at the larger scale of the whole western Mediterranean Basin a decrease in frequency of a smaller subset of events (strong and extreme) is also observed (Gkikas et al., 2013). Note that differences between both studies may come from different geographical location of interest: while Cachorro et al. (2016) concentrated on the north-central IP, Gkikas et al. (2013) used AERONET stations representative of the western basin in the southern

IP and northern Algeria.

As an idea of the low probability of occurrence of strong and extreme mineral dust events in winter, Gkikas et al. (2013) calculated the seasonal frequency of occurrence in the western Mediterranean Basin over land and for the period 2000–2007 of strong and extreme events to be 1 and 1.2%, respectively. In spite of this small percentage, two relevant strong and extreme (following the definition of Gkikas et al. (2013)) mineral dust events have been recorded in the last two years in the IP during the winter season. In February 2016 a strong event (AOD ~ 0.4) affecting the whole IP has been documented with in situ/remote sensing instrumentation (Titos et al., 2017), ceilometers (Cazorla et al., 2017) and in-situ/AERONET/satellite instrumentation (Sorribas et al., 2017). In February 2017 an exceptionally extreme event (AOD > 2.0) affected again the whole IP, as examined with AERONET and EARLINET/ACTRIS (European Aerosol Research Lidar Network/Aerosols, Clouds, and Trace gases Research InfraStructure Network) lidar data by Fernández et al. (2019), and the mineralogy of the event has been reported by Rodríguez-Navarro et al. (2018). According to AERONET (2018), this dust event is the strongest one over the IP since July 2012 and it is the strongest event (in terms of AOD) ever recorded over the IP during the month of February. According to Rodríguez-Navarro et al. (2018), the February 2017 event ended as "red rain" in several places in the IP, especially in the south, and accounted for most of the total yearly dust depositional flux to the IP. Such extreme events are thus of high significance to constrain input values, including dust composition, mineralogy, mixing state, and size, as well as depositional fluxes in dust and climatic models. Major effects of such extreme events impact the bioavailability of iron which is a key player in a range of global biogeochemical processes, especially over open ocean water (Jickells et al., 2005); and the aerosol direct radiative forcing since iron-containing particles strongly absorb solar and terrestrial radiations (Otto et al., 2007). In addition, they are relevant in health issues, as the abundance of inhalable, micrometer-sized fibers is associated with iron-rich nanoparticles (Rödelsperger et al., 1987; Nolan et al., 1991). Microorganisms carried by extreme dust events can be transported through the atmosphere and may affect human health and the functionality of microbial communities in various environments (Gat et al., 2017); and the increase of the PM10 levels as observed under Saharan dusty conditions is connected to the mortality in Spain (Díaz et al., 2017).

The assessment of dust model performance to predict the temporal evolution of mineral dust vertical distribution during such extreme events, as the one of February 2017, is rather rare in the literature (Huneeus et al., 2016, event with an AOD ~ 1.0; Ansmann et al., 2017, AOD ~ 0.6; Tsekeri et al., 2017, AOD ~ 0.4) as compared to single moderate events or long-term database of events independently of their intensity (Gobbi et al., 2013; Santos et al., 2013; Mona et al., 2014; Binietoglou et al., 2015; Sicard et al., 2015). These evaluations are usually made against vertically-resolved optical properties measured with lidar instruments. However, dust forecast models do not provide directly particle optical properties; instead, they simulate the life cycle with the microphysical properties assumptions (vertical flux, sedimentation, dry and wet deposition, convective mixing, etc.), and then diagnoses optical properties from the mass (Pérez et al., 2011). Optical properties are sub-products usually calculated from the modelled dust microphysics using Mie scattering theory (Pérez et al., 2006). This calculation is an additional source of error. In order to avoid it, it is thus preferable to compare the primary product of dust model, namely the mass concentration. Such attempts have been performed recently by Binietoglou et al. (2015) and Ansmann et al. (2017) with advanced, multi-spectral lidar systems employing either photometer/lidar synergetic algorithms such as the Lidar-Radiometer Inversion Code (LIRIC; Chaikovsky et al., 2016) or the Polarization Lidar Photometer Networking (POLIPHON; Mamouri and Ansmann, 2014, 2017), which is based on the particle depolarization ratio. Such algorithms are capable to estimate the vertical distribution of the dust mass concentration from the lidar-derived, vertically-resolved dust optical properties together with a few assumptions. The POLIPHON algorithm has been recently tested on lidar data of more simple systems, namely the one-wavelength elastic Polarized Micro-Pulse Lidars (P-MPL), as those routinely operating within the NASA Micro Pulse Lidar Network (MPLNET), to retrieve the optical properties separately for several types of particles in aerosol mixtures and proved to be reliable for particle types with moderate and strongly depolarizing properties such as mineral dust, smoke particles and pollen grains (Córdoba-Jabonero et al., 2018). However, as far as we know, POLIPHON has never been applied before to simple lidar systems for the retrieval of mass concentrations; for instance, POLIPHON has been applied to more complex lidar measurements from both the ground (e.g., Ansmann et al., 2011) and space (CALIPSO, Cloud-Aerosol Lidar and Infrared Pathfinder Satellite Observation) (Yu et al., 2015).

This work is based on the continuous observations of the vertical distribution of the extreme February 2017 mineral dust event by two P-MPL systems located in the north-east and central IP. The aim of the work regarding climate and environmental implications is twofold: 1) to demonstrate the potential of P-MPL or equivalent systems to retrieve the vertical distribution of mineral dust mass concentration in a full-time continuous mode; and 2) to evaluate the score of an operational dust regional forecast model in reproducing time-space evolution of mineral dust mass concentration profiling under those extreme dusty conditions.

2. Methodology

2.1. The extreme dust event and observational sites

The unprecedented, extreme dust intrusion which hit particularly strongly the IP in the western part of the Mediterranean Basin on 20–24 February 2017, has been documented in terms of the vertical distribution of the dust optical properties in Fernández et al. (2019) and in terms of its mineralogy by Rodríguez-Navarro et al. (2018). Lidar systems from the European Aerosol Research Lidar Network (EARLINET) from four stations in Portugal and Spain were used in Fernández et al. (2019). According to the latter, AOD at 675 nm peaked at 2.5 in Évora (Portugal), and Ångström exponents close to 0 were detected in all stations. Lidar ratios retrieved from night-time Raman measurements were found in the range of 40–55 sr at 355 nm and 34–61 sr at 532 nm. Mean particle depolarization ratios inside the dust plume were on the order of 0.26 and consistent between lidar stations. Fernández et al. (2019) also performed a model comparison with the NMMB/BSC-Dust model, the same model used in this work. In general terms, they found that 1) the model performed better in the north-eastern part of the IP than in its southwestern part, 2) the shape of the vertical distribution was better reproduced than the intensity of the event (correlation coefficient > 0.5), and 3) the model had a slight tendency to underestimate the observed optical properties. The lidar retrievals in Fernández et al. (2019) were based on the total (dust and non-dust) optical properties. In the present work, unlike to Fernández et al. (2019), the optical properties of the dust component (DD) alone are examined, once separated from the non-dust (ND) component, in addition to the mass concentration for dust particles, as described in the next section.

For that purpose, observations from two Spanish NASA/MPLNET (Micro Pulse Lidar NETwork) stations are examined during the two most intense days (22 and 23 February 2017) of the dust event. These two stations are: the Torrejón Observational Tower for Environmental Monitoring (TOTEM, 40.5°N 3.5°W, 680 m a.s.l.), located within the premises of the Instituto Nacional de Técnica Aeroespacial (INTA) at Torrejón de Ardoz (20 km far from Madrid, central IP), where temporarily MPLNET lidar measurements were carried out; and the Barcelona (BCN) site (NE IP, 41.4°N 2.1°E, 115 m a.s.l.), managed by the Universitat Politècnica de Catalunya (UPC). Fig. 1 shows their

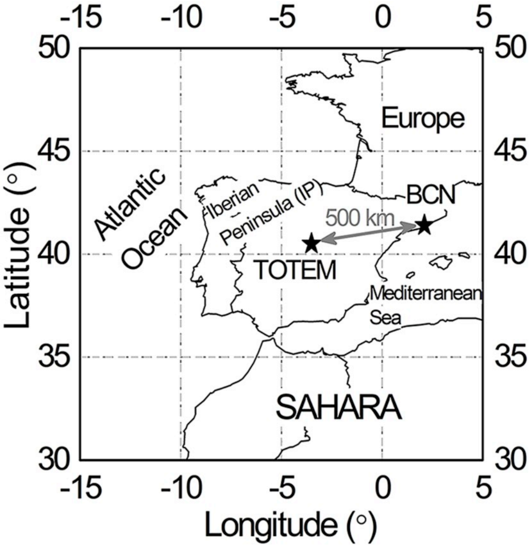

Fig. 1. Geographical location of the two lidar stations: TOTEM (40.5°N 3.5°W, 680 m a.s.l.) and BCN (41.4°N 2.1°E, 115 m a.s.l.); their relative distance is around 500 km.

geographical location at the IP, being their relative distance of around 500 km.

2.2. Polarized Micro-Pulse lidar (P-MPL) and AERONET measurements and retrievals

A polarized Micro-Pulse lidar (P-MPL), usually operating at the INTA/El Arenosillo site within the world-wide NASA MPLNET (mplnet.gsfc.nasa.gov), was temporarily deployed at TOTEM for vertical aerosol observations in the framework of the wintertime AVATAR (INTA research project for aerosol and gases monitoring) campaign. A similar P-MPL system is routinely operating in the permanent NASA/MPLNET site at BCN. The P-MPL system is an elastic lidar with a relatively high frequency (2500 Hz) using a low-energy (~7 μJ) Nd:YLF laser at 532 nm, including polarization capabilities. Vertical aerosol/cloud profiles are recorded in an automatic and continuous (24/7) mode, with a 0.5-min integrating time and 15-m vertical resolution. In order to increase the signal-to-noise ratio, those 0.5-min profiles are usually hourly-averaged.

The identification of dusty conditions, as described in Córdoba-Jabonero et al. (2011) requires: 1) the columnar Aerosol Optical Depth (AOD) and Angström exponent (AEx); and 2) HYSPLIT (Hybrid Single-Particle Lagrangian Integrated Trajectory model, HYSPLIT, 2018) back-trajectories for determining the origin of the dusty air masses. A first screening is based on moderate-to-high AOD (> 0.2) together to low AEx (< 0.5) corresponding to high aerosol load produced by large particles, likely dust. AERONET V2 L1.5 data from Madrid (20 km far from the TOTEM site) and Barcelona (AERONET, 2018), respectively operated by the Spanish Agencia Estatal de Meteorología (AEMET) and the Universidad Politècnica de Catalunya (UPC), were used in this work. The HYSPLIT model, developed by the NOAA's Air Resources Laboratory (ARL) (Draxler et al., 2009), was used together with the GDAS (Global Data Analysis System) meteorological files (spatial resolution of 0.5 × 0.5° every 3 h) as data input. Three-dimensional kinematic back-trajectories were calculated using the vertical wind component given by the meteorological model (Stohl, 1998); hourly back-trajectories with a 120 h pathway (5 days back) were computed.

Optical properties were derived from the AOD-constrained Klett-Fernald (KF) algorithm (Fernald, 1984; Klett, 1985): the total particle backscatter, β_p, and extinction, σ_p, coefficients (the vertical dependence is omitted for simplicity), and the Lidar Ratio (LR, the aerosol extinction-to-backscatter ratio), S_a. This procedure is based on the constraint of the vertically-integrated extinction coefficient, i.e., $\tau = \sum_z \sigma_p(z)\,\Delta z$ (Δz is the vertical resolution of the lidar profiles, and z denotes the height), to the AERONET AOD, if available, tuning the S_a value; otherwise, a fixed typical LR for dust ($S_a = 55$ sr) is used. The one-step POLIPHON approach is used for the separation of the height-resolved optical properties of the dust (DD) component, i.e., the vertical backscatter β_{DD} and extinction σ_{DD}, from the non-dust (ND) component (i.e., β_{ND} and σ_{ND}) in dusty mixtures. Note that the total β_p is the sum of β_{DD} and β_{ND} (likewise, $\sigma_p = \sigma_{DD} + \sigma_{ND}$). The general procedure of this method is described in detail in Mamouri and Ansmann (2017); a version specially applied to P-MPL measurements is widely explained in Córdoba-Jabonero et al. (2018), together with the errors associated to the retrieved parameters, as also shown in Table 1.

POLIPHON is based on the particle depolarization ratio, δ_p, for each specific pure component; in this work, δ_p values of 0.31 and 0.05 are assumed, respectively, for the DD and ND components (as in Córdoba-Jabonero et al., 2018). The estimation of the height-resolved mass concentration (MC, kg m^{-3}) of dust particles, $m_{DD}(z)$, is achieved by using a particular value of the Mass Extinction Efficiency (MEE, m^2 g^{-1}) for dust, k_{DD}, together with the lidar-derived dust extinction $\sigma_{DD}(z)$ (in km^{-1}), that is,

$$m_{DD}(z) = k_{DD}^{-1} \times \sigma_{DD}(z), \tag{1}$$

as described in Córdoba-Jabonero et al. (2018), where k_{DD} is obtained from the AERONET-derived total (particle coarse plus fine modes) mass conversion factors, c_v (10^{-12} Mm), and the particle density for dust ($\rho_d = 2.6$ g cm^{-3}), that is,

$$k_{DD} = \frac{1}{c_v \times \rho_d}, \tag{2}$$

being the mass conversion factor, c_v (10^{-12} Mm), defined as a function of the volume concentration, VC, and the AOD, τ, as:

Table 1
Errors derived for the P-MPL-derived optical properties (at 532 nm) and mass concentrations for dust. (n) and (d) stand for night-time and day-time P-MPL measurements, respectively.

Parameter	Symbol (*)	Errors	Comments
Dust backscatter coefficient (km^{-1} sr^{-1})	β_{DD}	5–20% (n) 10–30% (d)	(**)
Dust extinction coefficient (km^{-1})	σ_{DD}	10–30% (n) 15–40% (d)	Derived from the errors in β_{DD} and S_a
Lidar ratio (sr)	S_a	5–10%	Derived from KF algorithm
Particle linear depolarization ratio	δ_p	10–60%	(**)
Volume linear depolarization ratio	δ^V	10–50%	(**)
Mass Extinction Efficiency (m^2 g^{-1}) for dust	k_{DD}	0.01–0.10	Standard deviation (from the available AERONET data)
Mass concentration (g m^{-3}) for dust	m_{DD}	10–40%	Derived from the errors in σ_{DD} and k_{DD} (see Eq. (1))

(*) As denoted in the text.
(**) See Córdoba-Jabonero et al. (2018), and references therein.

$$c_v = \frac{VC}{\tau}. \tag{3}$$

Unfortunately, scarce AERONET data were available due to the presence of low clouds (even on 23 February, no AERONET data at Madrid and a single value at BCN is only provided); hence, a day-time averaged k_{DD} value obtained for the dusty observations on 22 February was applied for the dust extinction-to-mass conversion calculations: $k_{DD} = 0.57 \pm 0.01\,\mathrm{m^2\,g^{-1}}$ ($c_v = 0.68 \pm 0.01\ 10^{-12}\,\mathrm{Mm}$) for Madrid site (instead, this will be referred to TOTEM station, hereafter), and $k_{DD} = 0.87 \pm 0.10\,\mathrm{m^2\,g^{-1}}$ ($c_v = 0.45 \pm 0.05\ 10^{-12}\,\mathrm{Mm}$), for BCN. However, under more intense dusty conditions observed on 23 February in both stations (the dust impact was especially stronger at TOTEM w.r.t. BCN) the MEE was expected to be lower (predominance of larger particles) than that found for the previous day. This is also corroborated with the AERONET Fine Mode Fraction (FMF) values reported, respectively, at both stations, that is, 0.241 ± 0.004 and 0.37 ± 0.07, on 22 February, w.r.t. the FMF provided at BCN on 23 February: FMF = 0.11 (unfortunately, just a single value is reported, and no data at TOTEM). This rather low FMF value indicates the significant prevalence of coarse particles on 23 February. Therefore, due to the lack of AERONET data on 23 February, and in order to apply a suitable MEE for the extinction-to-mass conversion profiling on 23 February based on those results, the k_{DD} value is assumed from the mean c_v obtained on 22 February for the particle coarse mode only. Hence, a $k_{DD} = 0.47 \pm 0.01\,\mathrm{m^2\,g^{-1}}$ ($c_v = 0.83 \pm 0.01\ 10^{-12}\,\mathrm{Mm}$) and $k_{DD} = 0.66 \pm 0.05\,\mathrm{m^2\,g^{-1}}$ ($c_v = 0.58 \pm 0.05\ 10^{-12}\,\mathrm{Mm}$) are used, respectively, for TOTEM and BCN observations performed on 23 February 2017.

Indeed, all those k_{DD} are within typical MEE values for dust, i.e., from $0.35\,\mathrm{m^2\,g^{-1}}$ (coarser particles) to $2.0\,\mathrm{m^2\,g^{-1}}$ (finer particles), as reported by others authors (Yu et al., 2015; Córdoba-Jabonero et al., 2016, and references therein; Mamouri and Ansmann, 2017; Córdoba-Jabonero et al., 2018). In addition, regarding the OPAC (Optical Properties of Aerosols and Clouds) database (Hess et al., 1998) of the mass extinction efficiencies for specific aerosols, the difference found between those k_{DD} values obtained in both stations reflects that, at constant AOD, the dust volume concentration observed at TOTEM is enhanced (lower k_{DD}) w.r.t. the one at BCN (higher k_{DD}). This higher volume concentration of large particles is also accompanied by a lower mean AEx at TOTEM (AEx = 0.12 ± 0.04) w.r.t. BCN (AEx = 0.5 ± 0.2), as reported by AERONET on 22 February 2017; besides, a very low AEx of 0.04 (single value) is provided at BCN on 23 February (no data available at TOTEM on this day) (AERONET, 2018).

2.3. NMMB/BSC-dust model simulations

Forecasted profiles of both the extinction at 550 nm and the mass

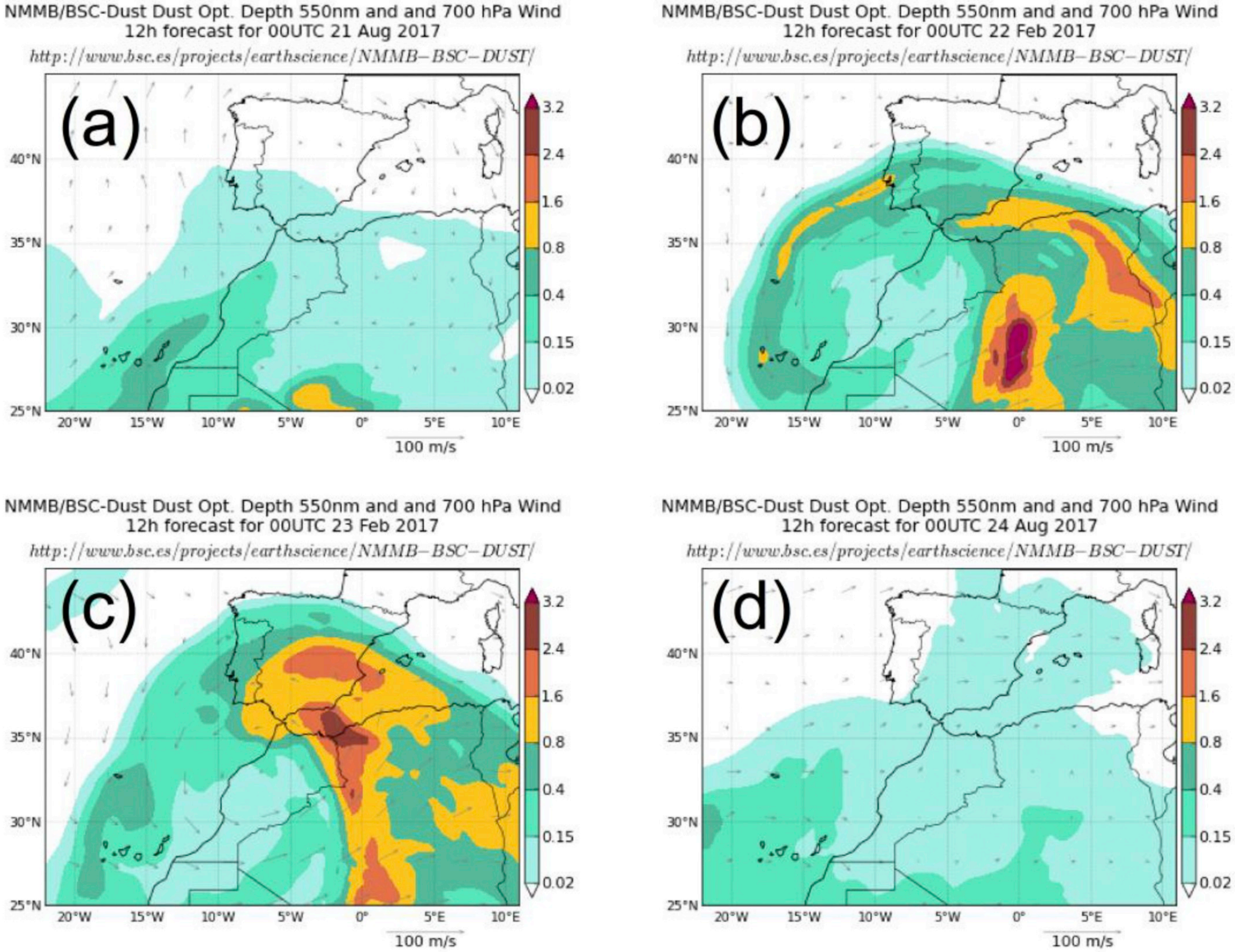

NMMB/BSC-Dust Dust Opt. Depth 550nm and and 700 hPa Wind
12h forecast for 00UTC 21 Aug 2017
http://www.bsc.es/projects/earthscience/NMMB−BSC−DUST/

NMMB/BSC-Dust Dust Opt. Depth 550nm and and 700 hPa Wind
12h forecast for 00UTC 22 Feb 2017
http://www.bsc.es/projects/earthscience/NMMB−BSC−DUST/

NMMB/BSC-Dust Dust Opt. Depth 550nm and and 700 hPa Wind
12h forecast for 00UTC 23 Feb 2017
http://www.bsc.es/projects/earthscience/NMMB−BSC−DUST/

NMMB/BSC-Dust Dust Opt. Depth 550nm and and 700 hPa Wind
12h forecast for 00UTC 24 Aug 2017
http://www.bsc.es/projects/earthscience/NMMB−BSC−DUST/

Fig. 2. NMMB/BSC-Dust mapping of the Dust Optical Depth at 550 nm and the 700-hPa Wind field at 12 h forecast for 00UT on (a) 21 February, (b) 22 February, (c) 23 February and (d) 24 February 2017 over the Spain domain.

concentration for mineral dust aerosol are obtained from the NMMB/BSC-Dust model. This model is developed and managed by the Barcelona Supercomputing Centre (BSC, www.bsc.es/ess/bsc-dust-daily-forecast), and provides operational forecasts of mineral dust for the Barcelona Dust Forecast Centre (BDFC, dust. aemet.es), the first specialized centre for prediction of mineral dust of the World Meteorological Organization (WMO).

The daily dust mass concentration forecasted profiles used in this study are based on the following operational setting of the BDFC model:

- The meteorological driver of the mineral dust model is the meteorological model Nonhydrostatic Multiscale Model on the B grid (NMMB) developed at the National Centers for Environmental Predictions (NCEP).
- Meteorological initial and boundary conditions used are NCEP/GFS data (0.5° × 0.5° horizontal resolution) at 12UT at intervals of 6 h.
- The horizontal resolution of the NMMB/BSC-Dust model is 0.1° × 0.1° (10 × 10 km) with a vertical resolution of 40 sigma-hybrid layers with the top of the atmosphere at 50 hPa.
- Model output is provided with a frequency of 3 h.
- There are 8 size bins from 0.1 to 10 μm following Pérez et al. (2011).
- The direct effect of the mineral dust on the radiation is considered.
- The mineral dust initial condition is based on the 24-h forecast from the previous day's model run.

Fig. 2 shows the intense dust intrusion that affected the IP and surroundings for the unusual wintertime dusty period of 21–24 February 2017, as 12-h forecasted for 00UT by the NMMB/BSC-Dust model, in terms of the Dust Optical Depth at 550 nm and the 700 hPa wind field (Fig. 2). The maximal dust impact can be observed occurring on 23 February 2017 (see Fig. 2c), affecting both the MPLNET TOTEM and BCN sites.

2.4. Comparative analysis: model forecasting vs lidar observations

Lidar-retrieved profiles of the mass concentration (see Sect. 2.2) were compared to those obtained from model simulations (see Sect. 2.3). Lidar observations are considered as point measurements with respect to the horizontal resolution, while the model simulations represent uniform pixels of 0.1° resolution (about 10 km wide). Regarding the temporal resolution, it should be taken into account that the lidar-retrieved profiles are hourly averaged (see Sect. 2.2) and the model-derived profiles are instantaneously results saved every 3 h (see Sect. 2.3). In this work, the comparison analysis between 'simultaneous' profiles is regarded between the modelled profile provided at time t and the lidar-derived profile obtained from the averaging of the two 1-h profiles retrieved at times t-1 and t. Therefore, eight dusty cases (profiling comparison) at the most can be compared for each day and station (32 cases in total: 2 days x 2 stations). However, due to the continuous presence of low clouds after around 19UT on 23 February at both stations, only 25 dusty cases could be examined (see next Sections).

Similarly to Fernández et al. (2019), the proposed comparative analysis is mainly based on the calculation of two specific parameters: the mean fractional bias, MFB, and the linear correlation coefficient, CC, acting as the usual statistical proxies used to evaluate the performance of the analysis between observations and models (Hanna et al., 1993; Chang and Hanna, 2004). The fractional bias, FB, is a normalized mean bias that indicates particularly systematic errors, regarding to an under- or over-estimation of the derived values. The CC represents a measure of the vertically-layered similarity between the observed and modelled profiles.

Due to the different vertical resolution between lidar and simulated profilings, the lidar-derived profiles were degraded to the fixed height-levels, z_i, provided by the model (40 levels in total). For the degradation, the profiles were height-averaged within specific intervals $[z_i - \Delta z_i,\ z_i + \Delta z_i]$, where Δz_i defines the half-width of each model height-level z_i, which ranges between the ground-level, z_1, and the top altitude, z_N, with dust detection (dust intrusions are observed not higher than 6 km, that is, $N = 20$). The half-width of each height-level, Δz_i, starting from the second one, is calculated as follows

$$\Delta z_{i+1} = [z_{i+1} - z_i] - \Delta z_i, \tag{4}$$

being $\Delta z_1 = z_1$ the half-width for the first level, z_1. Hence, the degraded lidar-derived mass concentrations were determined at each height-level z_i along the profile as height-averaged values within those intervals $[z_i - \Delta z_i, z_i + \Delta z_i]$; thus, the lidar profiling was obtained with the same vertical step layering of the model. For instance, the degree of degradation, as denoted by Δz_i, is depending on the height: on average, $\Delta z_i = 76 \pm 45$ m for heights less than 1.5 km, $\Delta z_i = 208 \pm 41$ m between 1.5 and 3.0 km height, and $\Delta z_i = 318 \pm 35$ m from 3.0 to 6.5 km.

The mean fractional bias, MFB, can be expressed as

$$MFB = \frac{1}{N}\sum_{i=1}^{N} FB(i) = \frac{1}{N}\sum_{i=1}^{N} 2 \times \left[\frac{\overline{X_{S\,i}} - \overline{X_{O\,i}}}{\overline{X_{S\,i}} + \overline{X_{O\,i}}}\right], \tag{5}$$

where i represents the model height-level z_i; X is the variable to be compared, i.e. the dust extinction, σ_{DD}, and/or the dust mass concentration, m_{DD}; and the sub-indexes S and O stand for the simulations and observations (measurements), respectively. The term $\bar{X}_i$ designs the vertically-averaged value for X within the height interval at level i, as previously explained. Likewise, the linear correlation coefficient, CC, is calculated for the $\overline{X_S}$ and $\overline{X_O}$ profiling datasets. As stated, this work is focused on the mass profiling, hence the selected X variable for the comparison analysis is the dust mass concentration, m_{DD}. The performance criteria of the comparison between simulations and observations can be considered acceptable for MFB values ranging from −0.6 to 0.6 (with a performance goal within ± 30%) (Kumar et al., 1993; Boylan and Russell, 2006), and CC values higher than 0.5, as considered a conservative value. In general, the degree of agreement of our comparative analysis will be based on the percentage of dusty profiling cases fulfilling those criteria w.r.t. all the dusty cases (25 in total).

Additionally, the centre-of-mass (CoM) height, Z_C, is also calculated for both lidar-degraded and modelled m_{DD} profiles, using a similar expression as shown in Mona et al. (2006), that is,

$$Z_c = \frac{\sum_{z_1}^{z_N} z_i\ \ m_{DD}(z_i)\ \ (2 \times \Delta z_i)}{\sum_{z_1}^{z_N} m_{DD}(z_i)\ \ (2 \times \Delta z_i)}, \tag{6}$$

representing the dust mass-weighted altitude, being m_{DD} the dust mass concentration at the height-level z_i (the symbol m_{DD} is unchanged for reading simplicity), Δz_i the half width of each height-level, and z_1 and z_N the ground-level and the top altitude as reached by the dust intrusion. The CoM height is determined for both the lidar-degraded and simulated m_{DD} profiles, and the criterion assumed for a comparatively good agreement between them is that their relative difference is lower than 15%, i.e., around 300 m at altitudes of 2000 m, as that obtained in other works (Mona et al., 2006; Fernández et al., 2019).

In addition, in order to evaluate probable discrepancies found at both lower and higher altitudes than Z_C, results are also examined regarding both the MFB and CC values as separately calculated for two layers: layer 1 (L1) from z_1 and Z_C, and layer 2 (L2) between Z_C and z_N.In addition, the dust mass loading (the vertically-integrated mass concentration, g m^{-2}), M_l, that is,

$$M_l = \sum_{z_1}^{z_N} m_{DD}(z_i)\ \ (2 \times \Delta z_i) \tag{7}$$

is also calculated for both the lidar-degraded and model-simulated mass concentration profilings. In this work, the selected comparative criterion of good agreement for M_l is that their relative difference is lower than 50% (i.e., around 0.5 μg m^{-2} w.r.t. 1 μg m^{-2}). Likewise, the percentage of dusty cases satisfying those criteria will reflect the degree of agreement.

In general, those parameters, MFB, CC, Z_c and M_l, have been used as proxies in order to evaluate the degree of agreement of the mass concentration profiles obtained from the NMMB/BSC-Dust simulations in comparison with the m_{DD} profiling as retrieved from P-MPL measurements.

3. Results

3.1. Lidar-derived dust optical properties: Dust component (DD) discrimination

Optical properties of the dust (DD) particles have been separated from those of the non-dust (ND) component using POLIPHON/P-MPL retrieval procedure (see Sect. 2.2; Córdoba-Jabonero et al., 2018) for the Saharan dust event occurred more intensely on 22 and 23 February 2017 over the two Spanish MPLNET TOTEM (temporary) and BCN (permanent) stations. The evolution of the lidar-derived AOD for the DD component, τ_{DD}, along those days at TOTEM and BCN (no data before 11UT on 22 February) is shown in Fig. 3. The dust incidence is observed over both sites, although dust intrusion is found to arrive later at BCN, from 15UT on 22 February. The highest dust impact ($\tau_{DD} > 1.5$) is detected on 23 February 2017, between 00UT and 02UT at TOTEM ($\tau_{DD} = 1.6 \pm 0.1$, in average), and from 04UT to 07UT at BCN ($\tau_{DD} = 1.7 \pm 0.1$, in average) (see Fig. 3). Despite AERONET data were scarce due to the unfortunate presence of low clouds for those days, the dust signature with extreme occurrence of large particles (i.e., high AOD and low AEx values, Córdoba-Jabonero et al., 2011) was observed at both sites. In particular, a mean (day-time averaged) AOD and AEx of 0.68 ± 0.09 and 0.12 ± 0.04, respectively, were provided at TOTEM on 22 February (unfortunately, no AERONET data on 23 February). In the case of BCN, low AEx values (0.5 ± 0.2) with a low mean AOD (0.13 ± 0.02) were observed on 22 February just from 15UT to 17UT, and a single high AOD and low AEx (2.0 and 0.04, respectively) were reported on 23 February. Note that AERONET provides day-time data only, and the higher dust incidence was observed later at night-times (see Fig. 3).

Regarding the lidar ratio (LR), retrieved values are within the typical S_a range for dusty conditions: 41–70 sr and 36–66 sr, respectively, for TOTEM and BCN. In average for those two days, a S_a of 61 ± 6 and 58 ± 10 sr is found, respectively, at TOTEM and BCN sites. In addition, particular features have been examined with HYSPLIT back-trajectory analysis (see Sect. 2.2 for details) of air masses arriving at particular altitudes in comparison with the vertical structure contribution of the dust particles (i.e., the DD component profiling) as observed at both sites.

About the vertical layered distribution of the optical properties for both the pure dust (DD) and non-dust (ND) components, a few dusty cases for TOTEM and BCN are illustrated, respectively, in Figs. 4 and 5. The particle backscatter coefficients (the total, β_p, and both the DD, β_{DD}, and ND, β_{ND}, components), together with the linear volume, δ^V, and particle, δ_p, depolarization ratios (left-side panels) are shown at several particular times on 22 and 23 February 2017 (dusty cases) for TOTEM (Fig. 4a and b, respectively) and BCN (Fig. 5a and b, respectively). δ_p values between 0.3 and 0.4 were mostly found, evidencing the occurrence of highly-depolarizing particles, likely coarse dust. HYSPLIT 5-day back-trajectories arriving at selected altitudes (as marked by coloured star symbols in Figs. 4 and 5, left-side panels) over each station on those selected dusty cases are also shown in the right-side panels of both figures.

In the case of TOTEM, the Saharan origin of the dust particles is confirmed: air masses coming from Saharan zones are arriving at altitudes above 1000 m a.g.l. on 22 and 23 February 2017 (see blue and green back-trajectories in Fig. 4-right panels), but also at lower heights on 22 February from 21UT on, hence transporting dust particles. This is also observed by the enhancement of both the DD backscatter, β_{DD} (see red line in Fig. 4-left panels), and δ_p profiles at those altitudes above the boundary layer (BL). However, the DD signature is also intensely found at the BL on 22 February before that is shown by HYSPLIT (see Fig. 4a-left at 15UT). This can be plausibly due to large particles coming from upper layers by gravitational settling, that is unable to be reported by HYSPLIT. In the case of BCN, the dust intrusion observed on 22–23 February 2017 is also coming from the Sahara area, regarding the HYSPLIT back-trajectory analysis. However, the Saharan air masses carrying dust particles are arriving over BCN on 22 February and the beginning of 23 February at high altitudes; later on 23 February, the Saharan air masses are completely coming at any altitude in overall. This is also reflected in the dust incidence observed along the two days over BCN (see Fig. 3): an enhancement of dust particles is detected just from 15UT on, being the highest dust impact on 23 February between 04UT and 07UT. This can be also seen in Fig. 5 (left-side panels), where the β_{DD} (and also δ_p) profiles show the DD signature (red line in Fig. 5) at altitudes higher than 1.0–1.5 km height on 22 February (and also observed on 23 February at 00UT; see red line in Fig. 5a and b), meanwhile ND aerosols (blue line in Fig. 5) are the only particles detected below around 1.0 km height. Later on, the β_{DD} is found distributed along all the profile on 23 February (in particular, β_{DD} profiles at 09UT and 15UT are shown in Fig. 5b). The enhanced presence of dust in the BL can be the result of the combination of the arrival of air masses carrying dust particles at those low heights and the additional loading due to large particles coming from upper layers by gravitational settling.

3.2. Dust mass concentration profiling: NMMB/BSC-dust forecast simulations vs. P-MPL retrievals

The comparative analysis was performed, as introduced in Sect. 2.4, between the predictions of the NMMB/BSC-Dust model and the P-MPL observations for the dust event observed on 22–23 February 2017 in terms of the vertical mass concentration of the dust particles. Lidar-degraded profiles of m_{DD} were estimated for the 25 available dusty cases: their optical properties could be retrieved (unfortunately, continuous cloudy conditions occurred at the end of 23 February at both stations), and derived at simultaneous-like times with the modelled mass profiles (forecast is performed every 3 h). The extinction-to-mass conversion procedure and the degradation process to model height-levels are described, respectively, in Sects. 2.2 and 2.4. In particular, 15 and 10 cases corresponded, respectively, to TOTEM and BCN observations. A few dusty cases are shown in Fig. 6 (the same corresponding to those shown in Figs. 4 and 5), which are also depicted together with the modelled mass concentration profiles (see Fig. 6a and b, respectively, for TOTEM and BCN cases).

In a first glance looking at Fig. 6a and b, a rather good vertical

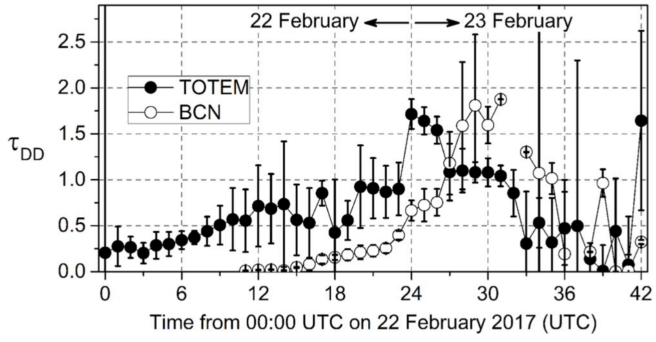

Fig. 3. Daily evolution of the lidar-derived AOD for the DD component, τ_{DD}, during 22 and 23 February 2017 at TOTEM (black circles) and BCN (white circles, no data before 11UT on 22 February) sites.

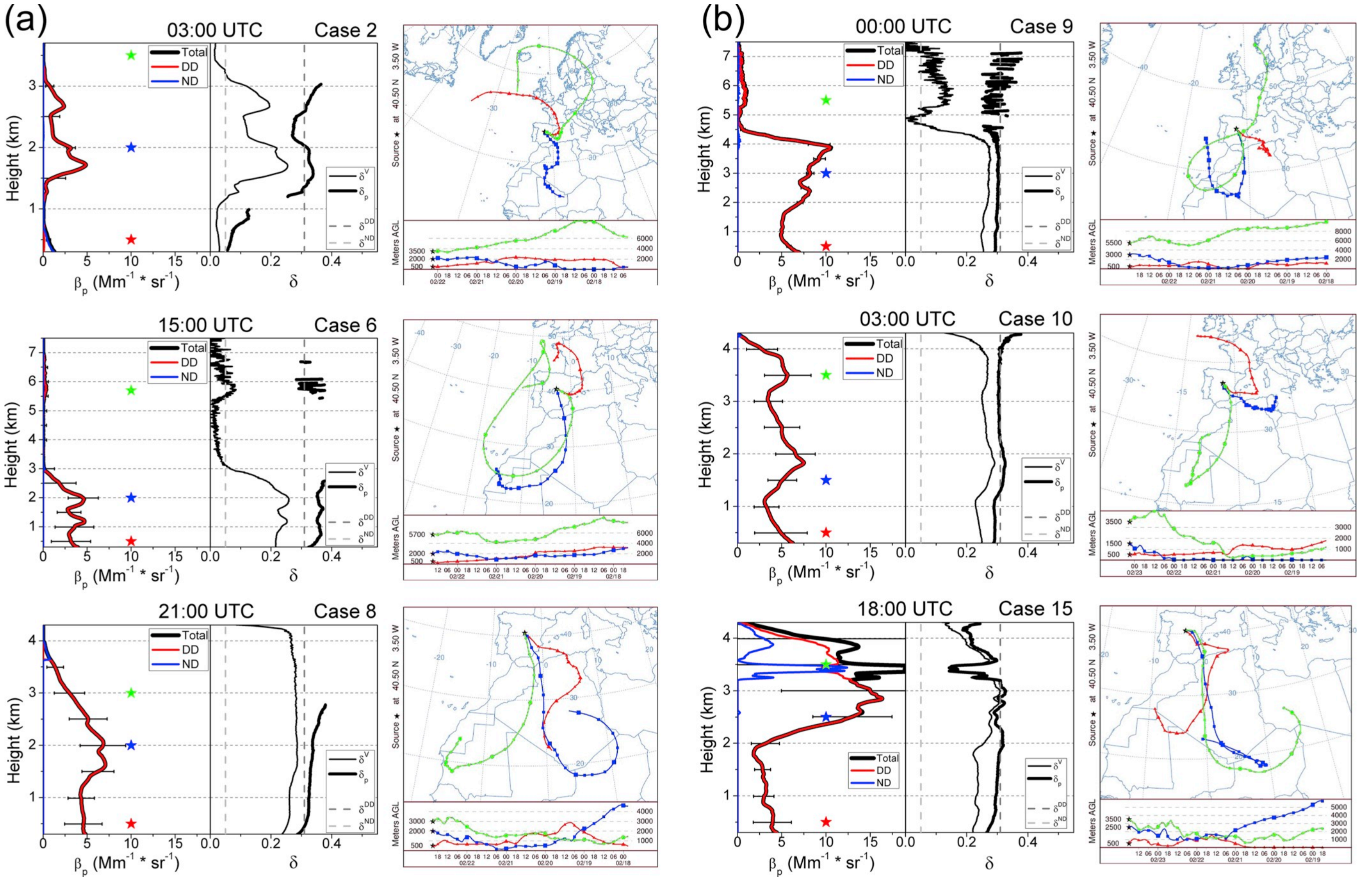

Fig. 4. Selected dusty cases (number is shown at the top of each plot) observed at the TOTEM station on (a) 22 February and (b) 23 February 2017. (Left-side panels) Profiles of (left) the backscatter coefficients: total backscatter (black) and their separated DD (red) and ND (blue) components, and (right) both the linear volume (δ^V, thin black) and particle (δ_p, thick black) depolarization ratios. Times are shown at the top of each plot. (Right-side panels) The corresponding HYSPLIT 5-day back-trajectories of the air masses arriving over TOTEM at the same times for three representative altitudes (as marked by coloured star symbols in the left-side plots). (For interpretation of the references to colour in this figure legend, the reader is referred to the Web version of this article.)

agreement is found between the lidar-degraded and the simulated dust mass concentration values. However, differences are mostly observed at low altitudes, when the dust intrusion started to arrive to the station. Indeed, lidar-derived results show no DD occurrence below 1.0–1.5 km height (only ND presence; i.e., see case 2 for TOTEM in Fig. 4a, and case 16 for BCN in Fig. 5a), while a relatively weak incidence is reported by the model (mainly marked for TOTEM, see case 2). Later on, the presence of dust is increasing at higher altitudes, as indicated by both the lidar measurements and the model simulations. In order to examine in more detail the relative performance between the P-MPL observations and NMMB-Dust simulations, a more comprehensive analysis have been achieved. For that purpose, as previously stated, the lidar-derived m_{DD} profiles were degraded to the height-levels of the model, and the *MFB* and *CC* parameters were calculated, as explained in Sect. 2.4. Results as obtained from this comparative analysis for the 25 dusty cases are shown in Table 2. In addition, the CoM height (Z_c, in km) and the mass loading for dust (M_l, in g m^{-2}) retrieved from lidar observations (*O*) and model simulations (*S*) together with their relative difference ($\Delta = \frac{[S-O]\times 100}{O}$, in %) were also calculated (see Table 2).

Regarding the degree of agreement between the model and lidar retrievals of the mass concentration for dust based on the *MFB* values, the percentage of favourable dusty cases fulfilling the performance criteria is 72%; likewise, similar values are obtained for each station (see Table 2). Among the favourable cases, the *MFB* is ranging between +0.45 (model overestimation) and −0.44 (model underestimation), representing an acceptable model performance (the best is for case 10, TOTEM at 03UT on 23 February, with a $MFB = 0.00$). However, that percentage decreases down to 60% and 56%, respectively, for the L1 and L2 layers. In particular, results show $|MFB| > 0.8$ in the L1, being all negative values (see Table 2) for cases 17–21 (from 18UT on 22 February to 06UT on 23 February) at BCN; hence, the percentage decreases down to 40% of favourable cases. This reflects that when the dust intrusion is arriving at BCN just before reaching the highest incidence (at around 05-06UT, see Fig. 3), the model largely underestimates the mass concentration in L1. In the case of TOTEM, this percentage is higher (degree of agreement of 73.3%); the model overestimates the mass concentration in L1 at early time up to 09UT on 22 February (cases 2–4), following an underestimation up to 06UT on 23 February (cases 5–11), once after the highest dust impact is reached (at around 01UT on 23 February, see Fig. 3).

By examining the results on *CC*, a high degree of similarity between the modelled and lidar-degraded vertical m_{DD} structures is found for 76% of the cases, with *CC* values ranging from 0.51 (case 8) to 0.97 (case 18) (only six cases present $CC < 0.5$, see Table 2). In addition, the degree of agreement, based on *CC* values, is really good in the L2 layer (96% of favourable cases), but being rather lower in L1 (only a 56% of favourable cases is found). Similar results are obtained, separately, for both TOTEM and BCN sites. This reflects the discrepancies of the mass concentration retrieved in the L1 layer between the dust model and the lidar observations.

The selected criterion for the relative CoM height differences (i.e., Δ_z lower than 15%) is satisfied for a 60% of all the cases, among those Δ_z varies between −11.4% and 14.6% (see Table 2); in particular, 66.7% of the favourable cases are obtained for TOTEM, lowering to a 50% for BCN. In general, the model-derived Z_c are higher than the lidar-derived ones (mostly positive Δ_z values). Regarding daily mean

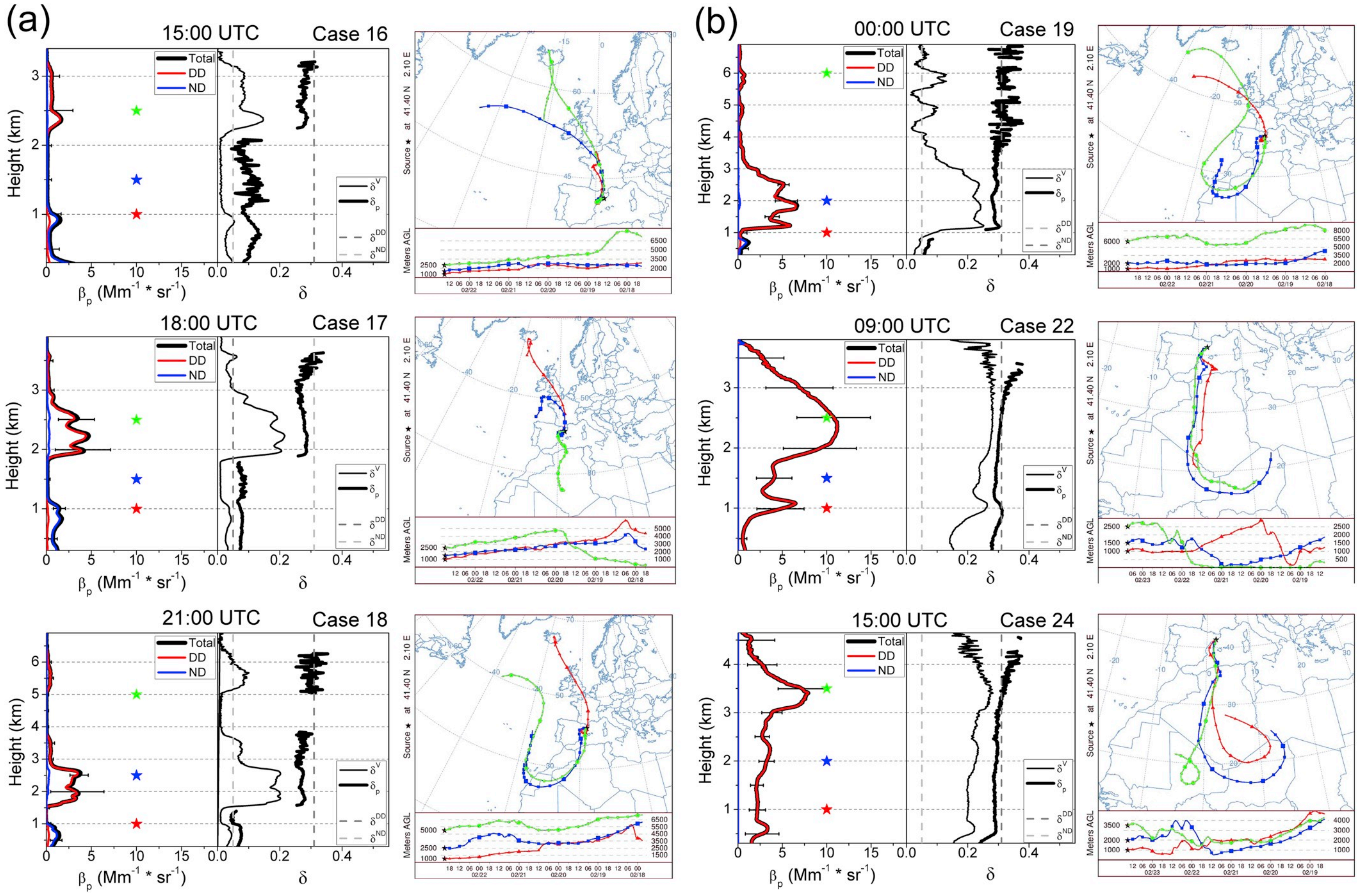

Fig. 5. The same as for Fig. 4, but for the BCN site (dusty case number is shown at the top of each plot). Note that the selected times (also shown at the top) and HYSPLIT back-trajectory arrival heights (as marked by coloured star symbols in the left-side plots) differ from those shown for the TOTEM profiles.

CoM height values, modelled Z_c derived at TOTEM is similar to that obtained from the lidar retrievals on 22 February ($Z_c = 1.8 \pm 0.3$ km), but differing in 400 m higher than the lidar-derived ones on 23 February ($Z_c = 2.2 \pm 0.4$ km). Likewise, calculations for BCN indicate a Z_c of 2.7 ± 0.1 and 2.3 ± 0.3 km on 22 February and 2.6 ± 0.2 and 2.2 ± 0.1 km on 23 February, as obtained, respectively, for the modelled and lidar-derived CoM height. This is mostly due to a poorer agreement of the mass profiling found in L1 at BCN w.r.t. TOTEM, as also reflected by the *MFB* and *CC* values for L1 (see Table 2). It should be noted that Z_c for the no-degraded lidar profiles is lower, a 1.9 ± 2.8% in average for all the cases, w.r.t. the degraded ones. These differences are rather low since the lidar-degraded averaging is performed within relatively large model intervals, Δz_i (318 ± 35 m), at altitudes from 3.0 to 6.5 km height, where the dust backscatter coefficient contribution is usually much lower than in the lower layer.

The relative differences of the mass loading, Δ_m, reveal a 60% of all the cases presents Δ_m lower than 50%; in particular, this percentage is slightly similar to that obtained for TOTEM (53.3%) and lower than that for BCN (70%). As previously stated, this can be due to the discrepancies found in the L1 between the model and lidar retrievals. Moreover, the evolution of the mass loading, M_l, along the two days 22 and 23 February, is rather similar up to 06UT on 23 February for the model simulations and the lidar observations at both stations, being the modelled M_l values generally higher and lower, respectively, than those lidar-derived ones at TOTEM and BCN, as shown in Fig. 7 (top panel). After that time, the M_l derived by the model is generally higher than that observed at both stations (see Fig. 7, top panel). All those discrepancies can be based on the uncertainties in the lidar retrievals, namely the separation of DD and ND components, the derived extinction coefficients by using a constrained/assumed lidar ratio, and the use of single extinction-to-mass conversion factors (and MEE) for each dusty day. Typical overall uncertainties in all presented parameters are discussed in Córdoba-Jabonero et al. (2018). In addition, the cloud contamination at the end of 23 February also affected the retrieval performance under those cloudy conditions, as stated before. However, the DD component is dominant for this extreme dust event, and the optimally constrained LR is found within the range of values that are typically assumed for dust. Hence, the most critical uncertainty in the mass concentration estimation arises from the single k_{DD} value used for each day in this work, as obtained from the AERONET daily-mean conversion factors (see Sect. 2.2). Indeed, an hourly-averaged k_{DD} would have been preferred. However, this is out of the scope of this work; available AERONET-derived k_{DD} were applied instead of the use of generalized climatological values for this (short) two-day dusty event (in fact, NRT was not an issue in this work).

While the relative M_l contribution to the L1, M_l^1 (in %), is mostly similar between the model and the lidar observations at TOTEM, M_l^1 is underestimated by the model w.r.t. the lidar retrievals at BCN, as shown in Fig. 7 (bottom panel). These results are also corroborated by other previous ones based on the model performance as examined using the *MFB* and *CC* parameters. By examining only observations, the contribution of the dust particles to the L1 layer ($z < Z_c$) can represent a maximum of 87.5% and 63.3% w.r.t. the total mass loading estimated, respectively, for TOTEM (case 5, 12UT on 22 February) and BCN (case 20, 03UT on 23 February), i.e., approximately 12 h later from the arrival of the dust intrusion over each station.

Finally, notice that the particular dust mass concentrations close to the surface at the TOTEM site (near Madrid) are above 500 μg m^{-3} (see Fig. 6a), with dust particles sized smaller than 10 μm. The World Health Organization (WHO) provides a reference database for ambient

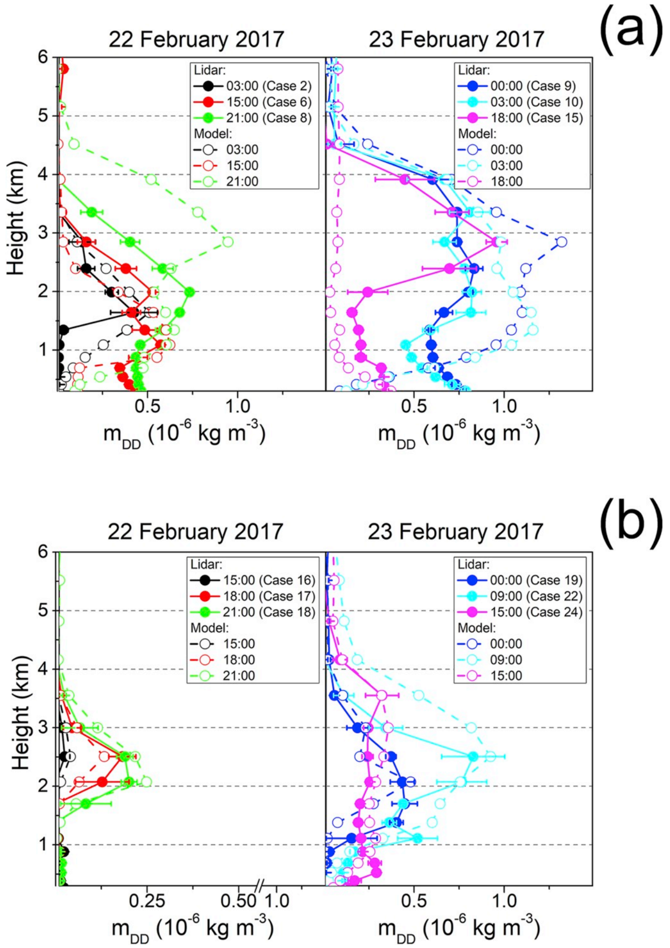

Fig. 6. Vertical dust mass concentration, m_{DD} (kg m^{-3}), as retrieved from the P-MPL lidar-degraded mass profiles for the DD component (solid-line/full-circles; standard deviation is also shown by error bars) and the NMMB/BSC-Dust model mass simulations for dust (dashed-line/open-circles), at (a) TOTEM and (b) BCN sites for those dusty cases shown in Figs. 4 and 5, respectively. Case numbers are shown in the legend.

(outdoor) air quality that consists mainly of urban air quality data annual means for PM10. The air quality levels under this particular extreme dust event temporarily reached values that are comparable to those observed regularly on other polluted megacities, such as Delhi or Great Cairo (WHO, 2018). For comparison, according to the WHO, the annually-averaged PM10 concentration measured at Torrejón de Ardoz (20 km from Madrid) for 2016 was 22 µg m^{-3}, and hence the February 2017 extreme dust event, as shown in this work, raised the surface level of particulates, PM10, by a factor of more than 20.

4. Conclusions

An extreme dusty event unusually occurred in wintertime over the Iberian Peninsula (IP) has been detected over two Spanish NASA/MPLNET sites: the temporary Torrejón Observational Tower for Environmental Monitoring (TOTEM, located at 20 km far from Madrid city, 40.5°N 3.5°W, 680 m a.s.l.) and the Barcelona station (BCN, at the Barcelona city centre, 41.4°N 2.1°E, 115 m a.s.l.). They both are placed at around 500 km distance each other. The highest dust incidence was observed from 22 to 23 February 2017. This two-day dusty scenario is examined in order to evaluate the NMMB/BSC-Dust model performance on forecasted mass concentration profiling in comparison with polarized Micro-Pulse (P-MPL) lidar-derived mass estimates for dust particles.

First, the separation of the optical properties of the dust (DD) from the non-dust (ND) component was achieved by using the combined P-MPL/POLIPHON method, retrieving the lidar-derived extinction profiles for the detached DD component, as described in Córdoba-Jabonero et al. (2018). Linear particle depolarization ratios between 0.3 and 0.4 were found, indicating the predominance of dust coarse particles. HYSPLIT back-trajectory analysis showed that air masses were coming from the Sahara region, with predominantly dust particles. The daily evolution of the dust intrusion along the two days showed a higher dust impact on 23 February, with maximums of the lidar-derived dust optical depth of 1.6 ± 0.1 between 00UT and 02UT and 1.7 ± 0.1 from 04UT to 07UT obtained, respectively, for TOTEM and BCN. Despite scarce AERONET data, Ångström exponents (AEx) of 0.12 ± 0.04 and 0.5 ± 0.3 were reported for TOTEM and BCN, respectively, indicating the dominant presence of larger dust particles over TOTEM than those observed at BCN. This can reflect the fact that dust particles reached TOTEM before than BCN (located at 500 km distance far from TOTEM), with a longer transport of dust particles, favouring the gravitational settling of coarser particles before reaching BCN, and hence lowering the predominance of large particles. The retrieved lidar ratios were within the typical values for dust: 61 ± 6 and 58 ± 10 sr were estimated, respectively, at TOTEM and BCN sites.

The extinction-to-mass conversion procedure as applied to the P-MPL measurements is based on the Mass Extinction Efficiency (MEE) for dust. The MEE values were obtained from the AERONET conversion factors under dusty conditions and the particle density for dust (ρ_d = 2.6 g cm^{-3}) (Mamouri and Ansmann, 2017; Córdoba-Jabonero et al., 2018). Reported mean MEE values at TOTEM were lower (0.57 ± 0.01 m^2 g^{-1}) than those found at BCN (0.87 ± 0.10 m^2 g^{-1}), showing the dust particles at TOTEM were predominantly larger than those observed at BCN, as also confirmed from AERONET AEx data. Profiles of the mass concentration (kg m^{-3}), and also the mass loading (g m^{-2}), of the dust particles (DD component) were calculated, and then compared with those forecasted by the NMMB/BSC-Dust model. For that purpose, a particular degradation of the lidar-retrieved mass profiles (25 available dusty cases) to the height-levels of the model was performed in order to have a similar vertical resolution in both lidar and model datasets. The number of available cases was limited due to cloud contamination preventing the lidar retrieval and the cadence of 3 h in the model forecasting for simultaneous comparisons. The comparative analysis performed was mainly based on two proxies: the Mean Fractional Bias, *MFB*, and the correlation coefficient, *CC*. The degree of agreement of the dust mass concentration profiling between the model and the lidar observations has been determined by the percentage of dusty cases satisfying the selected model performance criteria (favourable cases) of those two proxies. In general, by examining the *MFB* and *CC* results, a good agreement is found (72% and 76%, respectively, of favourable cases); however, large discrepancies are found at low altitudes between the dust model simulations and the lidar retrievals (those percentages decrease down to a 60% and 56% of favourable cases, respectively). These results are confirmed regarding the lidar-derived backscatter profiles at early stages of the dust intrusion arrival over each station: no evidence of dust signature at low altitudes ($<$ 1.0–1.5 km height); instead, only ND aerosols are observed.

In order to achieve a more comprehensive comparison, the centre-of-mass (CoM) height and the mass loading (ML) for both the modelled and lidar-derived dust mass concentration profiles were estimated for the 25 dusty cases, and their relative differences between datasets for both the CoM, Δ_z, and the ML, Δ_m, were also calculated. The mean lidar-derived CoM height of the dust event at TOTEM was found around 1.8 ± 0.2 and 2.2 ± 0.4 km, respectively, on 22 and 23 February; likewise, the CoM height was around 2.3 ± 0.3 and 2.2 ± 0.1 km at BCN, respectively, on those same days. By comparing those results with the modelled CoM heights, higher model-derived CoM height values were obtained in the 60% of the cases, being the difference criterion ($|\Delta_z| < 15\%$) fulfilled for the 66.7% and 50%, respectively, of the cases

Table 2
Lidar-derived dust extinctions, τ_{DD}, mean fractional bias, *MFB*, and correlation coefficients, *CC*, as obtained for all the 25 available dusty cases for TOTEM and BCN. The CoM height (Z_c, in km) and the mass loading (M_l, in g m^{-2}), as retrieved from lidar observations (*O*) and model simulations (*S*), together with their relative differences, Δ_z for the CoM height and Δ_m for the mass loading (in %), are also included.

Day of 2017	Time (UTC)	Case	τ_{DD}	*MFB* (**)			*CC* (**)			Z_c			M_l		
				L1 + *L2*	*L1*	*L2*	*L1* + *L2*	*L1*	*L2*	*O*	*S*	Δ_z	*O*	*S*	Δ_m
TOTEM station															
22 February	00:00	1	0.21	0.43	0.55	0.24	0.87	0.84	0.97	2.15	1.98	−8.0	0.36	0.90	148.1
	03:00	2 (*)	0.23	0.70	0.90	0.38	0.80	0.79	0.93	2.05	1.81	−11.4	0.41	0.72	74.2
	06:00	3	0.32	0.43	0.69	−0.36	0.87	0.88	0.88	1.75	1.63	−7.0	0.57	0.61	8.0
	09:00	4	0.47	0.23	0.22	0.26	0.86	0.82	0.99	1.65	1.67	0.9	0.84	0.73	−12.9
	12:00	5	0.63	−0.19	−0.31	−0.02	0.91	0.87	0.89	1.50	1.65	10.4	1.12	0.99	−11.8
	15:00	6 (*)	0.65	−0.74	−0.44	−1.18	0.77	0.67	0.96	1.70	1.52	−10.7	1.16	0.86	−26.2
	18:00	7	0.64	−0.18	−0.37	0.26	0.65	0.12	0.61	1.79	2.00	11.7	1.13	0.92	−19.2
	21:00	8 (*)	0.92	−0.07	−0.33	0.70	0.51	0.51	0.73	1.81	2.49	37.4	1.62	2.45	51.3
23 February	00:00	9 (*)	1.31	0.04	−0.16	0.25	0.65	−0.41	0.97	2.36	2.48	5.0	2.84	3.83	34.6
	03:00	10 (*)	1.31	0.00	−0.04	0.04	0.64	−0.15	0.97	2.48	2.41	−3.0	2.89	3.58	23.9
	06:00	11	1.08	−0.24	−0.31	−0.13	0.61	−0.34	0.92	2.32	2.51	8.1	2.34	2.43	4.0
	09:00	12	0.58	0.33	0.20	0.57	0.71	−0.52	0.95	2.14	2.49	16.2	1.26	2.10	67.6
	12:00	13	0.40	0.45	0.18	1.05	0.44	−0.83	0.79	1.80	2.51	39.2	0.85	1.92	125.0
	15:00	14	0.07	1.27	1.23	1.44	0.40	−0.55	0.75	1.56	2.47	58.1	0.16	1.50	845.7
	18:00	15 (*)	0.86	−0.82	−0.74	−0.99	0.06	0.85	−0.42	2.62	3.14	19.9	1.85	0.55	−70.6
BCN station															
22 February	15:00	16 (*)	0.03	0.45	0.29	0.68	0.44	−0.52	1.00	1.88	2.76	46.2	0.04	0.05	21.4
	18:00	17 (*)	0.14	−0.61	−0.82	−0.06	0.96	0.97	0.98	2.38	2.69	13.0	0.18	0.14	−23.2
	21:00	18 (*)	0.22	−0.44	−0.98	0.27	0.97	0.98	0.98	2.55	2.63	3.1	0.27	0.33	23.5
23 February	00:00	19 (*)	0.53	−0.74	−1.20	−0.14	0.81	0.81	0.84	2.39	2.59	8.1	0.87	0.65	−24.5
	03:00	20	0.97	−0.25	−1.23	0.73	0.79	0.88	0.91	2.17	2.66	22.7	1.57	1.21	−22.9
	06:00	21	1.70	−0.27	−1.17	0.77	0.83	0.82	0.97	2.15	2.69	24.9	2.75	2.04	−25.6
	09:00	22 (*)	1.30	−0.15	−0.45	0.75	0.82	0.89	0.89	2.10	2.72	29.8	1.41	2.28	62.2
	12:00	23	0.60	0.29	−0.31	1.19	0.47	0.35	0.98	2.15	2.82	31.3	0.98	1.95	98.6
	15:00	24 (*)	0.59	−0.01	−0.17	0.27	0.76	0.33	0.96	2.31	2.65	14.6	0.95	1.16	21.4
	18:00	25	0.17	0.90	0.88	0.92	0.38	−0.74	0.86	2.25	2.23	−0.8	0.28	0.76	169.6
Degree of agreement (%)				72	60	56	76	56	96			60			60

(*) Dusty cases shown in Figs. 4–6.
(**) *L1* + *L2*, *L1* and *L2* denote for the *MFB* and *CC* parameters as calculated for the overall profile (up to 6 km height) and for the L1 (z: z_1 - Z_c) and L2 (z: Z_c - z_N) layers separated, respectively, below and above w.r.t. Z_c (as described in the text).

examined at TOTEM and BCN. In general, modelled ML values were higher than those lidar-derived ones. However, the evolution of the mass loading along the two days, 22 and 23 February, was rather similar for both the model forecasting and lidar observations at both stations, at least, until 06UT on 23 February. The relative differences of the mass loading ($\Delta_m < 50\%$) represented a 60% of all the cases; and for $\Delta_m < 30\%$, a 56% of all the cases were favourable. The relative mass loading of dust particles in the L1 layer (< 2 km height, approximately) reached its maximum after 12 h later from the arrival of the dust intrusion over each station. Discrepancies can be based on the uncertainties in the lidar retrievals (the separation of DD and ND components, the derived extinction coefficients by using a constrained/assumed lidar ratio, and the use of single extinction-to-mass conversion factors) in addition to the cloud contamination at the end of 23 February affecting the retrieval performance under those cloudy conditions. Among those, the use of a single MEE value is the most critical source of uncertainties.

In general, a moderately good agreement is observed between P-MPL-derived dust mass concentration profiling and those mass profiles forecasted by the NMMB/BSC-Dust model at both sites. However, concerning lower altitudes, the comparative analysis showed large discrepancies. These can be plausibly due to a slower sedimentation of dust particles coming from upper layers by gravitational settling than that introduced by the NMMB/BSC-Dust model in the simulations; indeed, models tend to sediment coarse particles too fast (Basart, 2012).

Moreover, by comparing with the results shown in Fernández et al. (2019), the vertical mass concentration is better reproduced by the model than the vertical optical properties (i.e., the backscatter coefficients). This is mostly due to the fact that the mass concentration is a prime product of the model while the optical properties are derived, recalculated (with a certain number of assumptions) products. The especially good agreement between the modelled and observed mass concentration can be due to the particular nature of such extreme dust events, which transport predominantly pure dust particles with a rather low mixture with other aerosols. However, the agreement between the model estimates and the lidar observations could be poorer under weak and moderate dusty conditions. Indeed, the retrieval of the mass concentration for dust depends, besides the extinction-to-mass conversion factors, on the relative mixing state of Saharan air masses, that is, on their relative contribution of DD and ND aerosols. Hence, the level of uncertainty in the mass retrieval might increase for weak and moderate dust intrusions transporting more complex aerosol mixtures.

On the other hand, the extreme dust event shown in this work provided surface PM10 levels increased by a factor of more than 20, at least, w.r.t. the annually-averaged PM10 concentrations measured, for instance, at Torrejón de Ardoz (20 km far from Madrid) for 2016, according to the WHO. The air quality levels under this situation temporarily reached those observed values on other highly-polluted megacities, as Delhi or Great Cairo.

Finally, the methodology described for the dust model evaluation against the continuous P-MPL observations can be easily adopted by examining an extended period of weak, moderate and strong/extreme

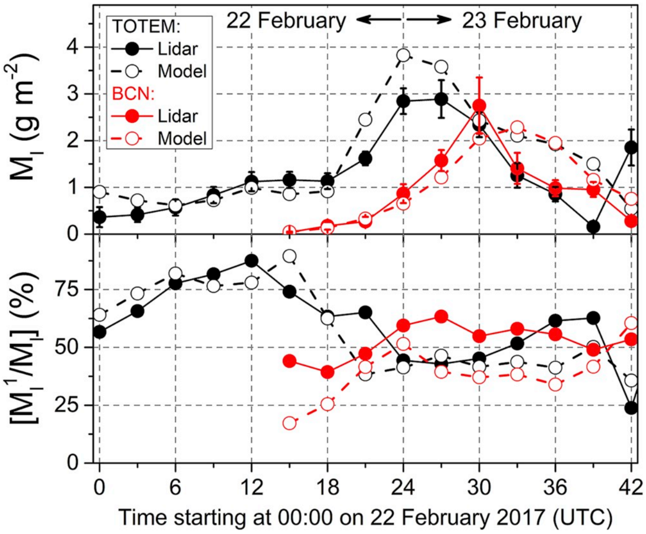

Fig. 7. (Top panel) Evolution of the mass loading, M_l (g m^{-2}), and (Bottom panel) the relative mass loading at the L1, M_l^1, w.r.t. the total M_l (in %) along 22 and 23 February 2017, as derived from the model simulations (open circles) and lidar observations (full circles) at TOTEM (black symbols) and BCN (red symbols) stations. Error bars correspond to the uncertainties obtained for the height-integrated lidar-derived m_{DD} (see Table 1). (For interpretation of the references to colour in this figure legend, the reader is referred to the Web version of this article.)

dust intrusions arriving to the Iberian Peninsula. Indeed, this extensive study would be especially valuable in order to consider an operational use of the NMMB/BSC-Dust model for forecasting the mass concentration profiling in frequently dust-affected regions with serious climate and environmental implications, as those covered by the prediction of the BDFC using the regional NMMB/BSC-Dust model (North Africa, the Middle East, Europe). However, typical MEE values for dust should be accurately specified, and hence, a statistical analysis for determining AERONET-based MEE values over the Iberian Peninsula is on-going.

Acknowledgements

This work was supported by the Spanish Ministerio de Economía y Competitividad (MINECO) under grant CGL2014-55230-R (AVATAR) and CGL2017-90884-REDT (ACTRIS-Spain); and the European Union's Horizon 2020 research and innovation programme under grant agreement n. 654109 (ACTRIS-2) and 778349 (GRASP-ACE). The MPLNET project is funded by the NASA Radiation Sciences Program and Earth Observing System. Lidar measurements in Barcelona were also supported by the Spanish MINECO (grant TEC2015-63832-P) and EFRD (European Fund for Regional Development), and by the Unidad de Excelencia María de Maeztu (MDM-2016-0600) financed by the Spanish Agencia Estatal de Investigación. The authors especially thank the Barcelona Supercomputing Centre and Dr. Sara Basart for providing simulation data from the NMMB/BSC-Dust model, and for their valuable comments on the results of the work. The authors also thank the AERONET PIs for their effort in establishing and maintaining Madrid and Barcelona sites, respectively operated by the Spanish Agencia Estatal de Meteorología (AEMET) and the Universidad Politècnica de Catalunya (UPC). The authors gratefully acknowledge the NOAA Air Resources Laboratory (ARL) for the provision of the HYSPLIT transport and dispersion model and/or READY website (http://www.ready.noaa.gov) used in this work. A. del Águila thanks the MINECO support (Programa de Ayudas a la Promoción del Empleo Joven e Implantación de la Garantía Juvenil en i + D + i) under grant PEJ-2014-A-52129.

Appendix A. Supplementary data

Supplementary data to this article can be found online at https://doi.org/10.1016/j.atmosenv.2019.116828.

References

AERONET, 2018. AERONET Aerosol Data Base. available at: http://aeronet.gsfc.nasa.gov/.

Alonso-Pérez, S., Cuevas, E., Querol, X., 2011. Objective identification of synoptic meteorological patterns favouring african dust intrusions into the marine boundary layer of the subtropical eastern North Atlantic region. Meteorol. Atmos. Phys. 113, 109–124. https://doi.org/10.1007/s00703-011-0150-z.

Ansmann, A., Tesche, M., Seifert, P., Groß, S., Freudenthaler, V., Apituley, A., Wilson, K.M., Serikov, I., Linné, H., Heinold, B., Hiebsch, A., Schnell, F., Schmidt, J., Mattis, I., Wandinger, U., Wiegner, M., 2011. Ash and fine-mode particle mass profiles from EARLINET-AERONET observations over central Europe after the eruptions of the Eyjafjallajökull volcano in 2010. J. Geophys. Res. Atmos. 116, D00U02. https://doi.org/10.1029/2010JD015567.

Ansmann, A., Rittmeister, F., Engelmann, R., Basart, S., Jorba, O., Spyrou, C., Remy, S., Skupin, A., Baars, H., Seifert, P., Senf, F., Kanitz, T., 2017. Profiling of Saharan dust from the Caribbean to western Africa - Part 2: shipborne lidar measurements versus forecasts. Atmos. Chem. Phys. 17, 14987–15006. https://doi.org/10.5194/acp-17-14987-2017.

Basart, S., 2012. Desert Dust Characterization in Northern Africa, Middle East and Europe through Regional Dust Modelling, and Satellite-Borne and Ground-Based Observations. PhD Thesis Dissertation. Barcelona Supercomputing Center/Centro Nacional de Supercomputación (BSC).

Bergametti, G., Gomes, L., Coudé-Gaussen, G., Rognon, P., Le Coustumer, M.N., 1989. African dust observed over Canary islands: source-regions identification and transport pattern for some summer situations. J. Geophys. Res. Atmos. 94, 14855–14864. https://doi.org/10.1029/JD094iD12p14855.

Binietoglou, I., Basart, S., Alados-Arboledas, L., Amiridis, V., Argyrouli, A., Baars, H., Baldasano, J.M., Balis, D., Belegante, L., Bravo-Aranda, J.A., Burlizzi, P., Carrasco, V., Chaikovsky, A., Comerón, A., D'Amico, G., Filioglou, M., Granados-Muñoz, M.J., Guerrero-Rascado, J.L., Ilic, L., Kokkalis, P., Maurizi Mona, L.A., Monti, F., Muñoz-Porcar, C., Nicolae, D., Papayannis, A., Pappalardo, G., Pejanovic, G., Pereira, S.N., Perrone, M.R., Pietruczuk, A., Posyniak, M., Rocadenbosch, F., Rodríguez-Gómez, A., Sicard, M., Siomos, N., Szkop, A., Terradellas, E., Tsekeri, A., Vukovic, A., Wandinger, U., Wagner, J., 2015. A methodology for investigating dust model performance using synergistic EARLINET/AERONET dust concentration retrievals. Atmos. Meas. Tech. 8, 3577–3600. https://doi.org/10.5194/amtd-8-3577-2015.

Boylan, J.W., Russell, A.G., 2006. PM and light extinction model performance metrics, goals, and criteria for three-dimensional air quality models. Atmos. Environ. 40, 4946–4959. https://doi.org/10.1016/j.atmosenv.2005.09.087.

Cachorro, V.E., Burgos, M.A., Mateos, D., Toledano, C., Bennouna, Y., Torres, B., de Frutos, A.M., Herguedas, A., 2016. Inventory of African desert dust events in the north-central Iberian Peninsula in 2003-2014 based on Sun-photometer-AERONET and particulate-mass-EMEP data. Atmos. Chem. Phys. 16, 8227–8248. https://doi.org/10.5194/acp-16-8227-2016.

Cazorla, A., Casquero-Vera, J.A., Román, R., Guerrero-Rascado, J.L., Toledano, C., Cachorro, V., Orza, J.A., Cancillo, M.L., Serrano, A., Titos, G., Pandolfi, M., Alastuey, A., Hanrieder, N., Alados-Arboledas, L., 2017. Near-real-time processing of a ceilometer network assisted with sun-photometer data: monitoring a dust outbreak over the Iberian Peninsula. Atmos. Chem. Phys. 17, 11861–11876. https://doi.org/10.5194/acp-17-11861-2017.

Chaikovsky, A., Dubovik, O., Holben, B., Bril, A., Goloub, P., Tanré, D., Pappalardo, G., Wandinger, U., Chaikovskaya, L., Denisov, S., Grudo, J., Lopatin, A., Karol, Y., Lapyonok, T., Amiridis, V., Ansmann, A., Apituley, A., Allados-Arboledas, L., Binietoglou, I., Boselli, A., D'Amico, G., Freudenthaler, V., Giles, D., Granados-Muñoz, M.J., Kokkalis, P., Nicolae, D., Oshchepkov, S., Papayannis, A., Perrone, M.R., Pietruczuk, A., Rocadenbosch, F., Sicard, M., Slutsker, I., Talianu, C., De Tomasi, F., Tsekeri, A., Wagner, J., Wang, X., 2016. Lidar-Radiometer Inversion Code (LIRIC) for the retrieval of vertical aerosol properties from combined lidar/radiometer data: development and distribution in EARLINET. Atmos. Meas. Tech. 9, 1181–1205. https://doi.org/10.5194/amt-9-1181-2016.

Chang, J.C., Hanna, S.R., 2004. Air quality model performance evaluation. Meteorol. Atmos. Phys. 87, 167–196. https://doi.org/10.1007/s00703-003-0070-7.

Córdoba-Jabonero, C., Sorribas, M., Guerrero-Rascado, J.L., Adame, J.A., Hernández, Y., Lyamani, H., Cachorro, V., Gil, M., Alados-Arboledas, L., Cuevas, E., de la Morena, B., 2011. Synergetic monitoring of Saharan dust plumes and potential impact on surface: a case study of dust transport from Canary Islands to Iberian Peninsula. Atmos. Chem. Phys. 11, 3067–3091. https://doi.org/10.5194/acp-11-3067-2011.

Córdoba-Jabonero, C., Andrey-Andrés, J., Gómez, L., Adame, J.A., Sorribas, M., Navarro-Comas, M., Puentedura, O., Cuevas, E., Gil, M., 2016. Vertical mass impact and features of Saharan dust intrusions derived from ground-based remote sensing in synergy with airborne in-situ measurements. Atmos. Environ. 142, 420–429. https://doi.org/10.1016/j.atmosenv.2016.08.003.

Córdoba-Jabonero, C., Sicard, M., Ansmann, A., del Águila, A., Baars, H., 2018. Separation of the optical and mass features of particle components in different aerosol mixtures by using POLIPHON retrievals in synergy with continuous polarized Micro-Pulse Lidar (P-MPL) measurements. Atmos. Meas. Tech. 11, 4775–4795. https://doi.org/10.5194/amt-11-4775-2018.

Díaz, J., Linares, C., Carmona, R., Russo, A., Ortiz, C., Salvador, P., Machado-Trigo, R.,

2017. Saharan dust intrusions in Spain: health impacts and associated synoptic conditions. Environ. Res. 156, 455–467. https://doi.org/10.1016/j.envres.2017.03.047.

Draxler, R.R., Stunder, B., Rolph, G., Taylor, A., 2009. Hysplit 4 User's Guide. NOAA Air Resources Laboratory, Silver Spring, MD, USA.

Escudero, M., Castillo, S., Querol, X., Avila, A., Alarcón, M., Viana, M.M., Alastuey, A., Cuevas, E., Rodríguez, S., 2005. Wet and dry African dust episodes over Eastern Spain. J. Geophys. Res. Atmos. 110 D18S08. https://doi.org/10.1029/2004JD004731.

Fernald, F.G., 1984. Analysis of atmospheric lidar observations: some comments. Appl. Opt. 23, 652–653. https://doi.org/10.1364/AO.23.000652.

Fernández, A.J., Sicard, M., Costa, M.J., Guerrero-Rascado, J.L., Gómez-Amo, J.L., Molero, F., Barragán, R., Basart, S., Bortoli, D., Bedoya-Velásquez, A.E., Utrillas, M.P., Salvador, P., Granados-Muñoz, M.J., Potes, M., Ortiz-Amezcua, P., Martínez-Lozano, J.A., Artíñano, B., Muñoz-Porcar, C., Salgado, R., Román, R., Rocadenbosch, F., Salgueiro, V., Benavent-Oltra, J.A., Rodríguez-Gómez, A., Alados-Arboledas, L., Comerón, A., Pujadas, M., 2019. Extreme, wintertime Saharan dust intrusion in the Iberian Peninsula: lidar monitoring and evaluation of dust forecast models during the February 2017 event. Atmos. Res. 228, 223–241. https://doi.org/10.1016/j.atmosres.2019.06.007.

Gat, D., Mazar, Y., Cytryn, E., Rudich, Y., 2017. Origin-dependent variations in the atmospheric crobiome community in eastern mediterranean dust storms. Environ. Sci. Technol. 51, 6709–6718. https://doi.org/10.1021/acs.est.7b00362.

Gkikas, A., Hatzianastassiou, N., Mihalopoulos, N., Katsoulis, V., Kazadzis, S., Pey, J., Querol, X., Torres, O., 2013. The regime of intense desert dust episodes in the Mediterranean based on contemporary satellite observations and ground measurements. Atmos. Chem. Phys. 13, 12135–12154. https://doi.org/10.5194/acp-13-12135-2013.

Gkikas, A., Basart, S., Hatzianastassiou, N., Marinou, E., Amiridis, V., Kazadzis, S., Pey, J., Querol, X., Jorba, O., Gassó, S., Baldasano, J.M., 2016. Mediterranean intense desert dust outbreaks and their vertical structure based on remote sensing data. Atmos. Chem. Phys. 16, 8609–8642. https://doi.org/10.5194/acp-16-8609-2016.

Gobbi, G., Angelini, F., Barnaba, F., Costabile, F., Baldasano, J.M., Basart, S., Sozzi, R., Bolignano, A., 2013. Changes in particulate matter physical properties during Saharan advections over Rome (Italy): a four-year study, 2001-2004. Atmos. Chem. Phys. 13 (15), 7395–7404. https://doi.org/10.5194/acpd-13-4963-2013.

Hanna, S.R., Chang, J.C., Strimaitis, D.G., 1993. Hazardous gas model evaluation with field observations. Atmos. Environ. 27A, 2265–2285.

Hess, M., Koepke, P., Schult, I., 1998. Optical properties of aerosols and clouds: the software package OPAC. Bull. Am. Meteorol. Soc. 79, 831–844. https://doi.org/10.1175/1520-0477(1998)079%3c0831:OPOAAC%3e2.0.CO;2.

Holben, B.N., Eck, T.F., Slutsker, I., Tanre, D., Buis, J.P., Setzer, A., Vermote, E., Reagan, J.A., Kaufman, Y., Nakajima, T., Lavenu, F., Jankowiak, I., Smirnov, A., 1998. AERONET - a federated instrument network and data archive for aerosol characterization. Remote Sens. Environ. 66, 1–16. https://doi.org/10.1016/S0034-4257(98)00031-5.

Huneeus, N., Basart, S., Fiedler, S., Morcrette, J.-J., Benedetti, A., Mulcahy, J., Terradellas, E., Perez-Garcia-Pando, C., Pejanovic, G., Nickovic, S., 2016. Forecasting the northern African dust outbreak towards Europe in April 2011: a model intercomparison. Atmos. Chem. Phys. 16 (8), 4967–4986. https://doi.org/10.5194/acp-16-4967-2016.

HYSPLIT, 2018. HYbrid Single-Particle Lagrangian Integrated Trajectory Model, Backward Trajectory Calculation Tool. available at: http://ready.arl.noaa.gov/HYSPLIT_traj.php https://doi.org/10.1175/BAMS-D-14-00110.1 and https://doi.org/10.1016/j.envsoft.2017.06.0.

Jickells, T.D., An, Z.S., Andersen, K.K., Baker, A.R., Bergametti, G., Brooks, N., Cao, J.J., Boyd, P.W., Duce, R.A., Hunter, K.A., Kawahata, H., Kubilay, N., LaRoche, J., Liss, P.S., Mahowald, N., Prospero, J.M., Ridgwell, A.J., Tegen, I., Torres, R., 2005. Global iron connections between desert dust, ocean biogeochemistry, and climate. Science 308, 67–71. https://doi.org/10.1126/science.1105959.

Klett, J.D., 1985. Lidar inversion with variable backscatter/extinction ratios. Appl. Opt. 24, 1638–1643. https://doi.org/10.1364/AO.24.001638.

Kumar, A., Luo, J., Bennett, G., 1993. Statistical evaluation of lower flammability distance (LFD) using four hazardous release models. Process Saf. Prog. 12 (1), 1–11. https://doi.org/10.1002/prs.680120103.

Liu, R., Liu, S.C., Cicerone, R.J., Shiu, C.-J., Li, J., Wang, J.L., Zhang, Y.H., 2015. Trends of extreme precipitation in Eastern Chine and their possible cause. Adv. Atmos. Sci. 32 (8), 1027–1037. http://doi.org/10.1007/s00376-015-5002-1.

Mamouri, R.-E., Ansmann, A., 2014. Fine and coarse dust separation with polarization lidar. Atmos. Meas. Tech. 7, 3717–3735. https://doi.org/10.5194/amt-7-3717-2014.

Mamouri, R.-E., Ansmann, A., 2017. Potential of polarization/Raman lidar to separate fine dust, coarse dust, maritime, and anthropogenic aerosol profiles. Atmos. Meas. Tech. 10, 3403–3427. https://doi.org/10.5194/amt-10-3403-2017.

Mona, L., Amodeo, A., Pandolfi, M., Pappalardo, G., 2006. Saharan dust intrusions in the Mediterranean area: three years of Raman lidar measurements. Journal of Geophysical Research-Atmospheres 111 (D16).

Mona, L., Papagiannopoulos, N., Basart, S., Baldasano, J., Binietoglou, I., Cornacchia, C., Pappalardo, G., 2014. EARLINET dust observations vs. BSC-DREAM8b modeled profiles: 12-year long systematic comparison at Potenza, Italy. Atmos. Chem. Phys. 14 (16), 8781–8793. https://doi.org/10.5194/acp-14-8781-2014.

Moreno, T., Querol, X., Castillo, S., Alastuey, A., Cuevas, E., Herrmann, L., Mounkaila, M., Elvira, J., Gibbons, W., 2006. Geochemical variations in aeolian mineral particles from the sahara–sahel dust corridor. Chemosphere 65, 261–270. https://doi.org/10.1016/j.chemosphere.2006.02.052.

Moulin, C., Lambert, C.E., Dayan, U., Masson, V., Ramonet, M., Bousquet, P., Legrand, M., Balkanski, Y.J., Guelle, W., Marticorena, B., Bergametti, G., Dulac, F., 1998. Satellite climatology of African dust transport in the Mediterranean atmosphere. J. Geophys. Res. Atmos. 103, 13137–13144. https://doi.org/10.1029/98JD00171.

Nolan, R.P., Langer, A.M., Herson, G.B., 1991. Characterisation of palygorskite specimens from different geological locales for health hazard evaluation. British J. Indust. Mineral. 48, 463–475. https://doi.org/10.1136/oem.48.7.463.

Otto, S., de Reus, M., Trautmann, T., Thomas, A., Wendisch, M., Borrmann, S., 2007. Atmospheric radiative effects of an in situ measured Saharan dust plume and the role of large particles. Atmos. Chem. Phys. 7, 4887–4903. https://doi.org/10.5194/acp-7-4887-2007.

Papadimas, C.D., Hatzianastassiou, N., Mihalopoulos, N., Querol, X., Vardavas, I., 2008. Spatial and temporal variability in aerosol properties over the Mediterranean basin based on 6-year (2000–2006) MODIS data. J. Geophys. Res. 113, D11205. https://doi.org/10.1029/2007JD009189.

Pérez, C., Nickovic, S., Baldasano, J.M., Sicard, M., Rocadenbosch, F., Cachorro, V.E., 2006. A long Saharan dust event over the Western Mediterranean: lidar, sun photometer observations and regional dust modelling. J. Geophys. Res. Atmos. 111, D15214. https://doi.org/10.1029/2005JD006579.

Pérez, C., Haustein, K., Janjic, Z., Jorba, O., Huneeus, N., Baldasano, J.M., Black, T., Basart, S., Nickovic, S., Miller, R., Perlwitz, J., Schulz, M., Thomson, M., 2011. Atmospheric dust modeling from meso to global scales with the online NMMB/BSC-Dust model - Part 1: model description, annual simulations and evaluation. Atmos. Chem. Phys. 11 (24), 13001–13027. https://doi.org/10.5194/acp-11-13001-2011.

Pey, J., Querol, X., Alastuey, A., Forastiere, F., Stafoggia, M., 2013. African dust outbreaks over the Mediterranean Basin during 2001–2011: PM10 concentrations, phenomenology and trends, and its relation with synoptic and mesoscale meteorology. Atmos. Chem. Phys. 13, 1395–1410. https://doi.org/10.5194/acp-13-1395-2013.

Prospero, J.M., Glacuum, R.A., Nees, R.T., 1981. Atmospheric transport of soil dust from Africa to South America. Nature 289, 570–572. https://doi.org/10.1038/289570a0.

Prospero, J.M., Ginoux, P., Torres, O., Nicholson, S.E., Gill, T.E., 2002. Environmental characterization of global sources of atmospheric soil dust identified with the Nimbus 7 Total Ozone Mapping Spectrometer (TOMS) absorbing aerosol product. Rev. Geophys. 40, 1–31. https://doi.org/10.1029/2000RG000095.

Querol, X., Alastuey, A., Puicercus, J.A., Mantilla, E., Miro, J.V., Lopez-Soler, A., Plana, F., Artiñano, B., 1998. Seasonal evolution of suspended particles around a large coal-fired power station: particulate levels and sources. Atmos. Environ. 32 (11), 1963–1978. https://doi.org/10.1016/S1352-2310(97)00504-9.

Querol, X., Pey, J., Pandolfi, M., Alastuey, A., Cusack, M., Moreno, T., Viana, M., Mihalopoulos, N., Kallos, G., Kleanthous, S., 2009. African dust contributions to mean ambient PM10 levels across the Mediterranean Basin. Atmos. Environ. 43 (28), 4266–4277. https://doi.org/10.1016/j.atmosenv.2009.06.013.

Rödelsperger, K., Brükel, B., Manke, J., Woitowitz, H.-J., Pott, F., 1987. Potential health risks from the use of fibrous mineral absorption granulates. Br. J. Ind. Med. 44, 337–343. https://doi.org/10.1136/oem.44.5.337.

Rodríguez, S., Querol, X., Alastuey, A., Kallos, G., Kakaliagou, O., 2001. Saharan dust contributions to PM10 and TSP levels in Southern and Eastern Spain. Atmos. Environ. 35, 2433–2447. https://doi.org/10.1016/S1352-2310(00)00496-9.

Rodríguez-Navarro, C., di Lorenzo, F., Elert, K., 2018. Mineralogy and physicochemical features of Saharan dust wet deposited in the Iberian Peninsula during an extreme red rain event. Atmos. Chem. Phys. 18, 10089–10122. https://doi.org/10.5194/acp-18-10089-2018.

Santos, D., Costa, M.J., Silva, A.M., Salgado, R., 2013. Modeling Saharan desert dust radiative effects on clouds. Atmos. Res. 127, 178–194. http://doi.org/10.1016/j.atmosres.2012.09.024.

Sicard, M., D'Amico, G., Comerón, A., Mona, L., Alados-Arboledas, L., Amodeo, A., Baars, H., Baldasano, J.M., Belegante, L., Binietoglou, I., Bravo-Aranda, J.A., Fernández, A.J., Fréville, P., García-Vizcaíno, D., Giunta, A., Granados-Muñoz, M.J., Guerrero-Rascado, J.L., Hadjimitsis, D., Haefele, A., Hervo, M., Iarlori, M., Kokkalis, P., Lange, D., Mamouri, R.E., Mattis, I., Molero, F., Montoux, N., Muñoz, A., Muñoz Porcar, C., Navas-Guzmán, F., Nicolae, D., Nisantzi, A., Papagiannopoulos, N., Papayannis, A., Pereira, S., Preißler, J., Pujadas, M., Rizi, V., Rocadenbosch, F., Sellegri, K., Simeonov, V., Tsaknakis, G., Wagner, F., Pappalardo, G., 2015. EARLINET: potential operationality of a research network. Atmos. Meas. Tech. 8, 4587–4613. https://doi.org/10.5194/amt-8-4587-2015.

Sicard, M., Barragan, R., Dulac, F., Alados-Arboledas, L., Mallet, M., 2016. Aerosol optical, microphysical and radiative properties at regional background insular sites in the western Mediterranean. Atmos. Chem. Phys. 16, 12177–12203. https://doi.org/10.5194/acp-16-12177-2016.

Sillmann, J., Poxxoli, L., Vignati, E., Kloster, S., Feichter, J., 2013. Aerosol effect on climate extremes in Europe under different future scenarios. Geophys. Res. Lett. 40, 2290–2295. http://doi.org/10.1002/grl.50459.

Sorribas, M., Adame, J.A., Andrews, E., Yela, M., 2017. An anomalous African dust event and its impact on aerosol radiative forcing on the Southwest Atlantic coast of Europe in February 2016. Sci. Total Environ. 583, 269–279. https://doi.org/10.1016/j.scitotenv.2017.01.064.

Stohl, A., 1998. Computation, accuracy and applications of trajectories - a review and bibliography. Atmos. Environ. 32 (6), 947–966. https://doi.org/10.1016/S1352-2310(97)00457-3.

Titos, G., Ealo, M., Pandolfi, M., Pérez, N., Sola, Y., Sicard, M., Comerón, A., Querol, X., Alastuey, A., 2017. Spatiotemporal evolution of a severe winter dust event in the western Mediterranean: aerosol optical and physical properties. J. Geophys. Res. Atmos. 122. https://doi.org/10.1002/2016JD026252.

Tsekeri, A., Lopatin, A., Amiridis, V., Marinou, E., Igloffstein, J., Siomos, N., Solomos, S., Kokkalis, P., Engelmann, R., Baars, H., Gratsea, M., Raptis, P.I., Binietoglou, I., Mihalopoulos, N., Kalivitis, N., Kouvarakis, G., Bartsotas, N., Kallos, G., Basart, S., Schuettemeyer, D., Wandinger, U., Ansmann, A., Chaikovsky, A.P., Dubovik, O., 2017. GARRLiC and LIRIC: strengths and limitations for the characterization of dust and marine particles along with their mixtures. Atmos. Meas. Tech. 10, 4995–5016. https://doi.org/10.5194/amt-10-4995-2017.

World Health Organization (WHO), 2018. Air Pollution Report: AAP Database. . http://www.who.int/airpollution/data/AAP_database_summary_results_2018_final2.pdf.

World Meteorological Organization (WMO), 2011. Weather Extreme in a Changing Climate: Hindsight on Foresight, WMO-No. 1075. (ISBN: 978-92-63-11075-6). https://library.wmo.int/pmb_ged/wmo_1075_en.pdf.

Yu, H., Chin, M., Bian, H., Yuan, T., Prospero, J., Omar, A.H., Remer, L., Winker, D., Yang, W., Zhang, Y., Zhang, Z., 2015. Quantification of trans-atlantic dust transport from seven-year (2007-2013) record of CALIPSO lidar measurements. Remote Sens. Environ. 159, 232–249. https://doi.org/10.1016/j.rse.2014.12.010.